

EFFECTS OF AGING ON MOUSE ROTATOR CUFF TENDON BIOMECHANICS

by

CHINMAY SAGAR PATWARDHAN

Presented to the Faculty of the Graduate School of The University of Texas at

Arlington in Partial Fulfilment

of the Requirements for the Degree of

MASTER OF SCIENCE IN BIOMEDICAL ENGINEERING

THE UNIVERSITY OF TEXAS AT ARLINGTON

December 2021

Abstract

Effects of Aging on Mouse Rotator Cuff Tendon Biomechanics

Chinmay Sagar Patwardhan, MS

University of Texas at Arlington, Bioengineering, 2021

Supervising Professor: Jun Liao

Rotator cuff tendon injuries and tear are caused by overuse, falling, or other accidents, and are often associated with old age. The severe injuries and tear can be debilitating and require nonsurgical treatment for partial tear and arthroscopic surgery for complete tear. The frequent location of injuries and tear are at the enthesis region, the interface where the tendon tissue gradually hardens and merges into the bone. Although aging has been identified as an important factor for rotator cuff tendon injuries and tear, how the mechanical properties of the bone-tendon complex evolve along with age is still a knowledge gap. Collaborating with the University of Nebraska Medical Centre, we have assessed the biomechanical properties of bone-rotator cuff tendon complex of male mice and female mice among various age groups (young: 2-3 months old, adult: 6-8 months old, and old: 15-18 months old). The failure stress, failure strain, and maximum tensile modulus were compared to reveal the overall trends among young, adult, and old groups, as well as female versus male. We found that, for failure stress (mechanical strength), no difference between young and adult mice was found, while old mice showed increased failure stress, especially the old male mice. The maximum tensile modulus represents the stiffness of the complex. An increasing trend was observed from young, to adult, to old mice, but only the difference between old male and young female groups was significant. No obvious trend exists in

the failure strain, except the complexes of young females had larger failure strains (more extensible) compared with the young male and adult male groups. Lastly, the male mice had higher overall failure stress than the female mice in adult and old groups, and the male mice had larger overall maximum tensile moduli than the female mice in all three age groups. Our mechanical data showed an interesting observation. The failure stress in the old group, especially the old male group, increased significantly compared to the young and adult groups. The maximum tensile modulus also showed an increasing trend from the young to old groups. Our observation in the mouse model indicates that age alone might not be the dominant risk factor to predict rotator cuff injury rate, and other factors associated with the aging process, like overuse, accumulated tissue damages/injuries, and underlying chronic disease, might contribute to the vulnerability of the rotator cuff in the elderly populations. We further performed Micro-CT imaging on the bone-tendon complex and reconstructed its 3D geometrical model using MITK, Slicer, and MeshLab software. With the material parameters obtained from the biomechanical tests, we successfully established a Finite Element Analysis model for the bone-rotator cuff tendon complex using ANSYS software and were able to simulate and demonstrate its age dependent mechanical behavior.

TABLE OF CONTENT

ABSTRACT	2
List of Illustrations	5
Chapter-1: Introduction	7
1.1 Background.	7
1.2 Literature Review.....	8
1.2.1 Review of Anatomy and Physiology	8
1.2.2 Biomechanical testing	12
1.2.3 3D reconstruction of CT scan images.....	17
1.2.4 Finite element analysis Simulation.....	20
Overview of research project	23
Chapter 2: Experimental Methods and Modeling Protocols.....	24
2.1. Apparatus	24
2.2. Procedure	25
2.2.1 Mechanical testing.....	25
2.2.2. Data Analysis... ..	27
2.2.3. 3D Modeling.....	28
2.2.4 FEA Simulation	43
Chapter-3: Results and Discussion.....	48
3.1. Mechanical Testing Results	48
3.2. ANSYS Simulation Results.....	50
3.3. Limitations and further improvements.....	54

3.4: Conclusions	55
References	57

LIST OF ILLUSTRATIONS

Figure-1: Similar anatomic structures of a rat and human models.....	10
Figure-2: (A) Mouse shoulder; (B) Human shoulder.....	10
Figure-3: Uniaxial mechanical testing machine.....	14
Figure-4: Stress–strain curves for various hyperelastic material models.....	17
Figure-5: MITK workbench used for 3D reconstruction.....	19
Figure-6: Mouse bone-rotator cuff tendon complex.	26
Figure-7: Test-Resources sample clamps. and mounted sample immersed in PBS bath	27
Figure-8: Polyethylene strip was attached to reinforce the muscular end of the tendon.....	28
Figure-9: Preview of the reconstructed tendon model using 3D slicer software.....	30
Figure-10: The geometry is imported as a non-editable graphic due to its large size and complexity.....	32
Figure-11: Before Laplacian smoothening.....	34
Figure-12: After Laplacian smoothening with self-intersecting face selected.....	34
Figure-13: After quadratic edge collapse decimation.....	35
Figure-14: The anatomy of tendon-muscle interface shown by Micro-CT image.....	36
Figure-15: Tendon imported as a non-editable graphic due to extreme complexity.....	37
Figure-16: Simplified tendon model.....	38
Figure-17: Final simplification in MeshLab.....	38
Figure-18: Default geometry of the bone after reconstruction.....	40
Figure-19: Bone geometry with unnecessary parts removed.....	41
Figure-20-A: Final bone model.....	42
Figure-20-B: Actual bone for comparison.....	42
Figure-21-A: Bone-tendon integrated model.....	43
Figure-21-B: Bone-tendon sample for comparison.....	43
Figure-22: Tendon-Bone geometry imported in ANSYS design modeler workspace.....	44
Figure-23: Tendon model after meshing is complete.....	45

Figure-24: The bone-rotator cuff tendon complex under uniaxial tensile mechanical testing.....	46
Figure-25: Comparison of actual test setup and virtual simulation.....	46
Figure-26: ANSYS workbench setting for simulation.....	47
Figure-27: Failure stress-strain curves for all samples.....	49
Figure-28: Von Mises stress plot generated from FE simulation of the bone-rotator cuff tendon complex of young female and male mice.....	52
Figure 29: Von Mises stress plot generated from FE simulation of the bone-rotator cuff tendon complex of adult female and male mice.....	53
Figure 30: Von Mises stress plot generated from FE simulation of the bone-rotator cuff tendon complex of old female and male mice.....	54

LIST OF TABLES

Table 1: A breakdown of the composition, location, and orientation of various connective tissues that are associated with the shoulder joint.....	12
Table 2: Failure stress of the bone-rotator cuff tendon complex.....	50
Table 3: Failure strain of the bone-rotator cuff tendon complex.....	50
Table 4: Maximum tensile modulus of the bone-rotator cuff tendon complex.....	50

CHAPTER 1: INTRODUCTION

1.1 Background

The work on this thesis began in conjunction with a collaborative research with the University of Nebraska Medical Center (UNMC), when the author was tasked with conducting tensile mechanical testing of mouse shoulder rotator cuff tendons for a project entitled: “Effects of maturation and aging on the rotator cuff tendon-to-bone interface”¹.

The scope of that project was in conducting histological and biochemical analyses of specimens to find how collagen content, proteoglycan deposition, collagen fiber orientation, and other biofactors affect the enthesis mechanics. The biomechanical testing of the bone-rotator cuff tendon complex is thus of importance to assess the age-dependent alterations in mechanical properties and would help effectively establish a correlation between the composition/microstructure of the enthesis and its altered mechanical behavior along with maturation and aging.

After the accomplishment of mechanical testing of mouse bone-rotator cuff tendon complexes of various age groups, the author took further efforts to perform 3D geometrical reconstruction of the bone-tendon complex from Micro-CT images using MITK, Slicer, and MeshLab software. The goal is to establish a 3D reconstruction protocol for mouse shoulder bone-rotator cuff tendon complex, as well as a Finite Element (FE) model using ANSYS software for in-depth simulation and analysis. FE model has the strength to simulate and predict mechanical behavior of tissue or organs under various loads and complicated boundary conditions². The establishment of 3D reconstruction and FE modeling protocols, along with our biomechanical testing

capacity, would build a strong biomechanical analysis platform for future sophisticated studies of shoulder bone-rotator cuff tendon complex, helping understand the effect of age, sex, and various diseases.

In short, in this MS thesis research the author has successfully carried out the biomechanical testing of bone-rotator cuff tendon complex of male mice and female mice among various age groups (young: 2-3 months old, adult: 6-8 months old, and old: 15-18 months old). The biomechanical testing results helped reach an important conclusion that age alone might not be the dominant risk factor to predict rotator cuff injury rate, and other factors associated with the aging process, like overuse, accumulated tissue damages/injuries, and underlying chronic disease, might contribute to the vulnerability of the rotator cuff in the elderly populations¹. Moreover, with the Micro-CT images and material parameters obtained from the biomechanical tests, the author has successfully established a 3D reconstruction protocol and an FE model for the bone-rotator cuff tendon complex. The FE model was able to simulate and demonstrate the age dependent mechanical behavior of the bone-tendon complex.

1.2. Literature Review

1.2.1. Review of Anatomy and Physiology

I. Similarities between human and mouse shoulder rotator cuff tendons

Mouse and rat models have been studied for over a century because the physiology is similar to that of humans, they possess similar set of muscles in the shoulder region and the structure is similarly constructed as well.

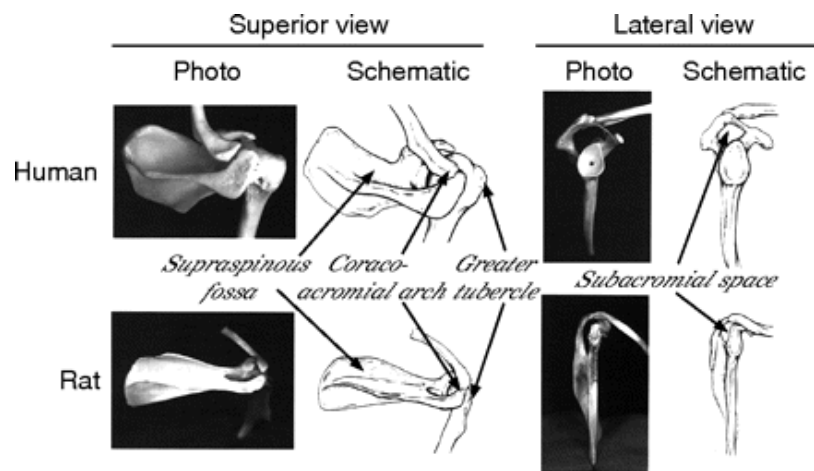


Figure 1: Similar anatomic structures of a rat and human models.

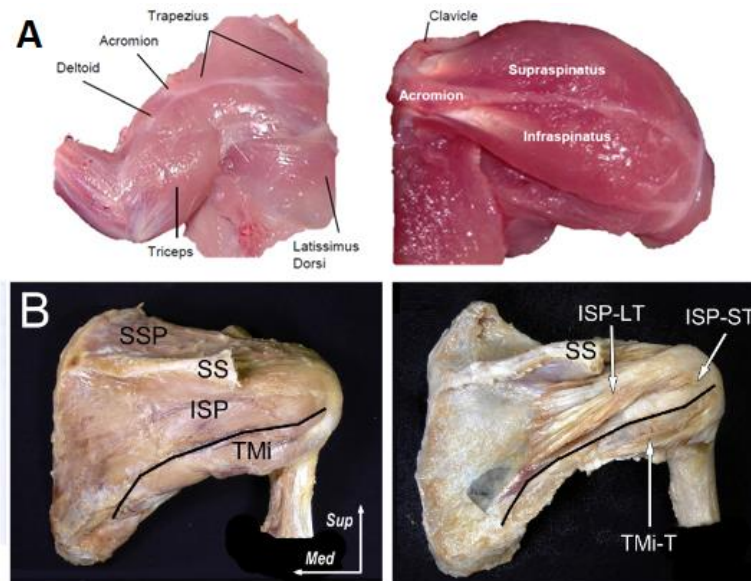


Figure 2: (A) Mouse shoulder³; (B) Human shoulder⁴.

II. Anatomy of rotator cuff muscles/tendons and their respective functions

The rotator cuff in both humans and mice/rats consists of the following shoulder-joint stabilizing muscle groups:⁵

- 1) **Subscapularis** - Makes particular movements of abduction and extension of shoulder muscle possible by facilitating internal rotation of the humerus. Its function is dependent on position of the arm, and is only called into action when the arm is raised, that it pulls the humerus forward and downward.
- 2) **Supraspinatus** - Offers resistance to gravitational pull acting on the shoulder supraspinatus is therefore actively involved in initiating of shoulder abduction. As stated by Wattanaprakornkul et al. in 2011, "Posterior rotator cuff muscles appear to be counterbalancing anterior translational forces produced during flexion and it would appear that supraspinatus is one of the muscles that consistently initiates flexion".
- 3) **Infraspinatus** - This is the primary external rotator of the shoulder joint assisting in producing shoulder extension. Its involvement is conditional to the arm being fixed upon which it abducts the inferior angle of the scapula.
- 4) **Teres minor** – When the humerus is stabilized, it works in combination with infraspinatus for making external rotation of the shoulder joint possible by abducting the inferior angle of the scapula.

From the anatomy of muscle function stated above, it is clear that the supraspinatus tendon is the only one involved in every possible motion of the arm, and is continuously in an “active mode”. Theoretically, as long as an

organism is alive and mobile, its limbs are constantly under the effect of gravity. For this reason, we focused on the study of supraspinatus rotator cuff tendon, and the testing specimens consisted of only the supraspinatus rotator cuff tendon as the sole attachment between the bone and muscle, while the other groups of tendons were removed along with the muscles attached to them.

Table 1: A breakdown of the composition, location, and orientation of various connective tissues that are associated with the shoulder joint¹.

Region	Cells	Arrangement	Collagen Composition
Tendon	Tenocytes	Linearly arrayed	Type I collagen Type III collagen
Mineralized fibrocartilage	Hypertrophic Fibrochondrocytes	Localized gradient	Type II collagen Type X collagen
Non-mineralized fibrocartilage	Fibrochondrocytes	Localized gradient	Type II collagen Type III collagen
Bone Tissue	Osteoblasts Osteocytes Osteoclasts	Matrix	Type I collagen Type III collagen

The bone-rotator cuff tendon complex used for tensile mechanical testing had singular supraspinatus tendon as the attachment between the bone and the attached muscle. However, the CT scans we took was from intact shoulder and hence the image of surrounding muscles and other tendons/ligaments increased the complexity, which asked attention to distinguish the supraspinatus tendon from the surrounding tissues.

III. Aging and tendon injuries.

Rotator cuff tendon injuries are common musculoskeletal ailments and prevalent causes of shoulder pain and joint disorders⁶. The injuries are associated with more than 4.5 million physician visits and 40,000 surgical treatments annually in the United States^{7 8}. The observed trend shows that the rate of injuries increases with aging⁹. Anomalies are observed in around 9.7% of individuals up to 20 years old, while it increases to 62% in patients over 80 years old¹⁰. Even with advanced therapeutic methods, the retear rate for all age groups is ~7%, and increases to 25% for patients over the age of 70^{11 12}.

1.2.2. Biomechanical testing

I. Uniaxial tensile mechanical testing



Figure 3: Uniaxial mechanical testing machine.

The mechanical assessment of the bone-tendon complex was carried out by conducting uniaxial tensile mechanical testing. The test involves subjecting the specimen to a controlled tensile displacement along a single axis, the change in dimensions and resulting load is then recorded to calculate a stress-strain curve, which is utilized to determine the structural or material properties. Before subjecting the bone-tendon complex to uniaxial tensile testing, preconditioning need to be performed. Preconditioning applies repeated loading and unloading cycles to the soft tissues so as to achieve repeatable loading and unloading curves. The preconditioning is essential to overcome the effects of soft tissue handling history and establish a repeatable set of experiments. The preconditioning procedure orientates the internal microstructures of soft tissues to its natural in vivo alignment and hence resulting in more consistent data from mechanical testing^{13 14}.

The initial gauge length, tendon width, and tendon thickness were measured using a Mitutoyo digital caliper. The displacement and load were recorded by machine grip-to-grip distance and load cell, respectively. The engineering stress and engineering strain were computed via the following formulae:

$$\epsilon_e = \Delta L/L_o \quad (1)$$

where ϵ_e is the engineering strain, ΔL is the tendon deformation calculated from the displacement, L_o is the initial gauge length of the tendon.

$$\sigma_e = F/A_o \quad (2)$$

where σ_e is the engineering stress, F is the external tensile load applied on the tendon, A_o is the average initial cross-sectional area of the tendon.

Some of the important concepts and terminologies for biological sample uniaxial tensile testing were discussed below.

II. Biomechanical behavior of tendon tissues and hyperelasticity

Tendons are soft tissues¹⁵ predominantly composed of hierarchically organized collagen and arranged parallel to the long axis of the tendon, resulting in high tensile strength¹⁶. As observed by Lopez-Capos et al¹⁷, tendons tend to exhibit nonlinear pseudoplastic behavior, which results in a nonlinear stress-strain curve with large deformation. The nonlinearity and extremely large deformation can be described and treated by hyperelastic constitutive model. When treated as an elastic material, the stress measured at a particle \mathbf{X} will be a function of the current deformation gradient \mathbf{F} related to that particle. The stress-strain

relationship of the elastic material can then be defined as:

$$\mathbf{P} = \mathbf{P}(\mathbf{F}(\mathbf{X}), \mathbf{X}) \quad (3)$$

Where \mathbf{X} is coordinates of the particle at the initial position, \mathbf{F} is the current deformation gradient associated with that particle, \mathbf{P} is measured first Piola–Kirchhoff stress ¹⁸

During the deformation, the stresses will do work to the material. If the work done by the stresses is only dependent on the initial configuration at time t_0 and the final confirmation at time t , this material behavior can be described as path-independent (i.e., only initial and final configurations matter) and defined as hyperelasticity. The path-independency of hyperelastic material can be treated with the following functions that related the strain energy function Ψ (elastic potential) to \mathbf{P} and deformation gradient \mathbf{F} [18]:

$$\Psi(\mathbf{F}(\mathbf{X}), \mathbf{X}) = \int_{t_0}^t \mathbf{P}(\mathbf{F}(\mathbf{X}), \mathbf{X}) : \dot{\mathbf{F}} dt \quad (4)$$

$$\dot{\Psi} = \mathbf{P} : \dot{\mathbf{F}} \quad (5)$$

Where Ψ is the strain energy function per unit undeformed volume, \mathbf{X} is coordinates of the particle at the initial position, \mathbf{F} is the deformation gradient, \mathbf{P} is the measured first Piola–Kirchhoff stress [18].

More compact forms can be used to define hyperelastic materials as follows.

$$\mathbf{P}(\mathbf{F}(\mathbf{X}), \mathbf{X}) = \frac{\partial \Psi(\mathbf{F}(\mathbf{X}), \mathbf{X})}{\partial \mathbf{F}} \quad (6)$$

Where Ψ is the strain energy function per unit undeformed volume, \mathbf{X} is coordinates of the particle at the initial position, \mathbf{F} is the deformation gradient, \mathbf{P} is the measured first Piola–Kirchhoff stress [18].

$$\mathbf{S}(\mathbf{C}(\mathbf{X}), \mathbf{X}) = \frac{\partial \Psi(\mathbf{C}(\mathbf{X}), \mathbf{X})}{\partial \mathbf{E}} \quad (7)$$

Where Ψ is the strain energy function per unit undeformed volume, \mathbf{X} is coordinates of the particle at the initial position, \mathbf{C} is the right Cauchy–Green deformation tensor, \mathbf{E} is the green strain tensor, \mathbf{S} is the second Piola–Kirchhoff stress [18].

As we described above, hyperelastic material¹⁹ is a type of constitutive model for ideal elastic material, for which the stress–strain relationship derives from a strain energy function. In simple words it is the stress-strain behavior of hyperelastic materials is elastic but highly nonlinear²⁰. The deformation of most hyperelastic materials, remains elastic up to large strain values.

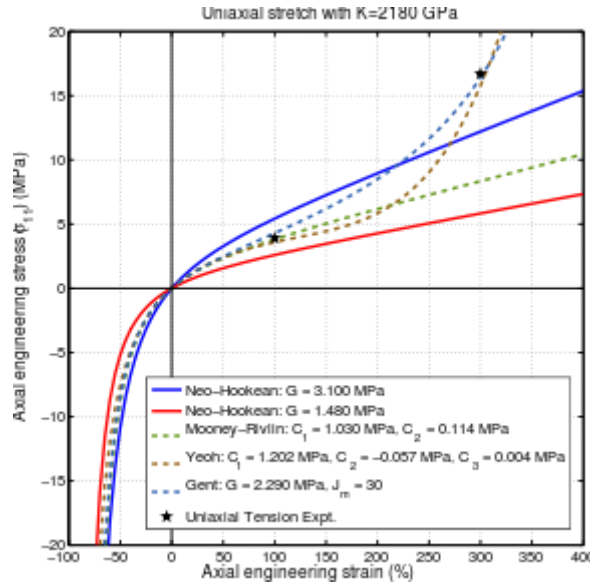


Figure 4: Stress–strain curves for various hyperelastic material models²¹.

The following assumptions are made when modeling a hyperelastic material:

- 1) The material behavior is elastic.
- 2) The material behavior is isotropic.

- 3) The material is nearly incompressible (Poisson's ratio is 0.475 by default).

The material coefficients of the hyperelastic models can be derived from curve fitting. When experimental result from uniaxial testing or biaxial testing is entered into ANSYS software, and a model is picked from various material models, such as Mooney-Rivlin, Ogden, and Yeoh Arruda-Boyce, to best reflect the trend of the curves, the coefficients can be generated with the curve fitting function of the software.

1.2.3 3D reconstruction of Bone-Tendon Complex

I. Generation of 3D models from CT scan dataset.

A standard view of MITK workbench that is used for conversion of image data sets to 3D models is depicted in Figure 5. The common steps involved in all such applications are importing the image in the software, isolating the region of interest, using segmentation technique to delineate the anatomical features, generating a .stl file, exporting the file for post-processing.

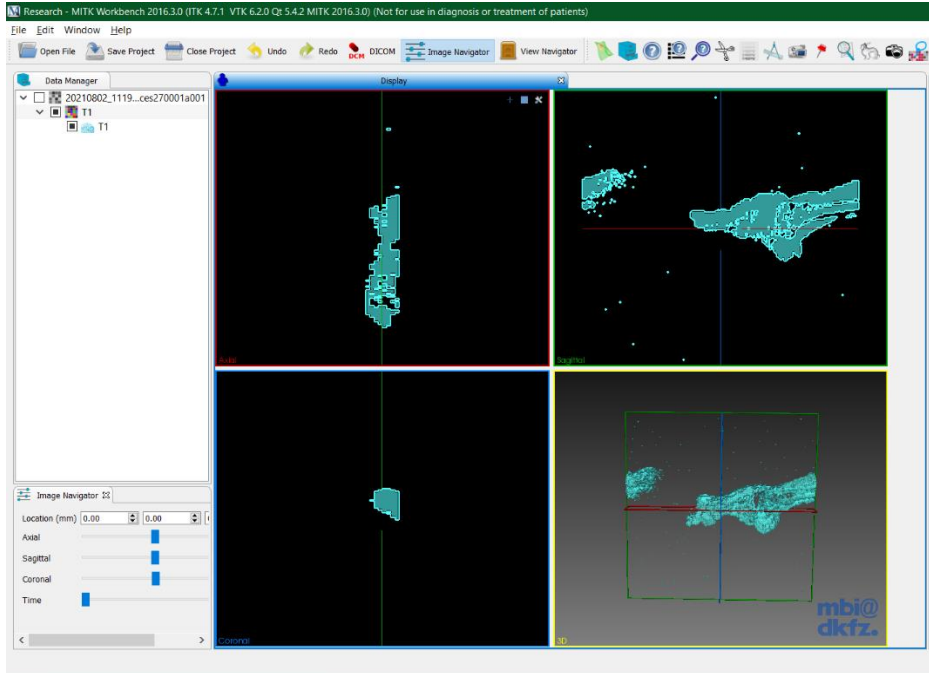


Figure 5: MITK workbench used for 3D reconstruction.

II. Consideration in segmentation²²

Segmentation is an imaging processing step to distinguish and mark the regions of interest in the images, which reflect the anatomical features, structures, lesions, and various other objects in the spatial environment. It is a very common procedure in medical image computing, required for visualization of certain structures, measuring volumetric, surface and shape properties for eventual 3D printing, and masking. The specifics of the number of segments and the pixel size of final image can be customized. Segmentation can be manual, by individually looking at all the slices of an image data set and drawing a contour at the boundary, or an automatic boundary which useful when the area of interest has a high contrast to the surroundings; the former method is time consuming and an automatic method might not always be applicable, and therefore a semi-automatic or hybrid segmentation procedure is carried out. Segment Editor module offers a wide range of segmentation

methods. Simpler models require less time to analyze, but are inaccurate, while denser models require higher processing power to achieve a higher resolution.

III. Smoothing

Smoothing of the 3D model is an essential step to remove noises ²³so that the model appears more anatomical accurate. Effective smoothing in MeshLab, to manage the triangle density requires vertices to exist at a density greater than the features to be smoothed. therefore, in the absence of adequate number of triangles, smoothing cannot be implemented. Triangle splitting is necessary for smoothing a densely meshed body, followed by smoothing, the process is repeated until the body becomes as crease free as one desires. The repeated approach is necessary because smoothing would be ineffective if there are no larger densely meshed surfaces. During the iteration, the splitting operation makes the mesh finer by generating required number of triangles, and then smoothing can reduce the creases. Note that during each iteration, vertices, half-edges, and triangles are dynamically created and deleted to achieve simplification and smoothing. ²⁴

Smoothing is a common technique that is available in all image processing and 3D modeling platforms the module specific to 3D slicer functions by filling in holes and removing extrusions, the option to smooth all segments smoothens all visible segments in order of file list. the list of functions available in this module are given below²⁵-

- Median: Remove small extrusions and fills small gaps while keeps smooth contours mostly unchanged. Applied to selected segment only.
- Opening: Remove extrusions smaller than the specified kernel size. Does not add

anything to the segment. Applied to selected segment only.

- Closing: Fill sharp corners and holes smaller than the specified kernel size. Does not remove anything from the segment. Applied to selected segment only.
- Gaussian: Smoothen all details. Strong smoothing as achievable, but tends to shrink the segment. Applied to selected segment only.
- Joint smoothing: Smoothen multiple segments at once, preserving watertight interface between them. If segments overlap, segment higher in the segments table will have priority. Applied to all visible segments.

1) **Duplicate entities**

In any 3D model composed of multiple objects, the boundary between two separate objects is composed of shared vertices. Once such a model is edited, these shared vertices might break and recombine to form duplicate vertices, duplicate faces, and other geometric entities that add unnecessary noise to the model. This is a frequent occurrence, especially during scaling operations. Therefore, removing duplicates is an essential step in model optimization and an efficient strategy before it is loaded into the GPU.²⁶

2) **Remove unreferenced vertices**

It is recommended to apply this filter last, as other functions tend to remove the triangles but not the vertices, and some might tend to inadvertently generate such entities as a result of performing their designated task. Therefore, it is the most efficient way to use this cleaning method as the final step.

Closing hole and building a patch of triangles tends to produce several undesired auto-collisions. To avoid them, the following filter sequence is quite effective.

Select Border→Laplacian Smooth→Close Holes

If the problem persists, the noisy faces in the boundary can be discarded by:

Select Border→Delete selected faces→Select Border

→Laplacian Smooth→Close Holes

1.2.4. Finite element analysis simulation using ANSYS workbench

1) Mooney-Rivlin 2 parameter hyperelastic model

This is the constitutive equation used for predicting the nonlinear stress-strain behavior of elastic materials undergoing large deformations. The stress-strain curve is initially linear, but at a certain point it deviates. The assumption for such materials is that neo-Hookean model does not account for the dissipative energy as heat during material straining and perfect elasticity is assumed at all stages of deformation²⁷. Moreover, to choose the appropriate material model, one must check the strain rate. If it is within 30%, Neo-Hookean model suffices; but for levels over 200%, Mooney-Rivlin or Ogden are better. The strain rate for tendons was 92%, which is why our choice for constitutive model was Mooney-Rivlin model²⁸.

It is important to understand that Mooney-Rivlin model does not give any special insight into material behavior. The model is merely curve fitting using polynomial formula to the stress-strain data. The numerical values of

coefficients derived from the curve fitting are then used in FEA programs²⁹ for use in mechanical analyses. The FEA program knows how stiff the material is at certain strain based on the values of the coefficients. In short, the hyperelastic model depends on the mathematical formula and the material coefficients derived from curve fitting. When experimental test results such as uniaxial, biaxial etc. are entered in ANSYS the coefficients are generated, which are then used to determine the behavior of the material generated.

2) **Mesh Convergence**

As a numerical technique to simulate a physical phenomenon, Finite Element Method (FEM) uses mathematical equations for successful quantification of physical phenomena such as material deformation, wave propagation, or fluid flow. Due to the infinite Degrees of Freedom (DOF) possessed by any continuous object in the real world, it is impossible to perform manual calculations of partial differential equations (PDE) that are used to define an object and its state. FEM employs creation of a mesh that splits the domain into a discrete number of elements, of which the solutions can be calculated. The solution data is then interpolated across the whole domain³⁰. It is always recommended to perform a mesh convergence study, where the same problem is solved many iterations with a denser mesh each time, and the results are compared; if the results show mesh independence and additional mesh refinement is unnecessary, the FEA model is said to converge to a solution and be accurate.³¹

3) **Large Deflections in ANSYS**

The inclusion of large deflection means that ANSYS accounts for changes in stiffness due to changes in shape of the parts you are simulating, since hyperelastic materials exhibit almost instantaneous elastic response to large strains³². During the simulation, the large deflection effect option is turned on to realize the simulation of Mooney-Rivlin model. Without it, the simulation is constrained to a linear equation, and will show no variation in strain response with change in its shape.³³

CHAPTER 2: EXPERIMENTAL METHODS AND MODELING PROTOCOLS

2.1. Apparatus

Mechanical Testing

- 1) Test-Resources Uniaxial testing device
- 2) Mouse shoulder rotator cuff specimens
- 3) Polymer strips
- 4) Superglue
- 5) Vernier calipers, ruler, markers

3D modelling and FEA simulation

- 1) CT scan data of bone-rotator cuff complex
- 2) 3D slicer software
- 3) MeshLab software
- 4) Autodesk fusion 360
- 5) Solidworks
- 6) ANSYS work bench

There were five samples from each of the following groups, young female (YF), adult female (AF), Old female (OF), young male (YM), adult male (AM) and old male (OM), the total number of samples tested were 30.

2.2. Procedure

2.2.1 Mechanical testing

- 1) The samples arrived in a frozen state due to overnight shipping. The samples were composed of a humerus bone attached to the shoulder muscle via the supraspinatus tendon, which is the focus of our study.

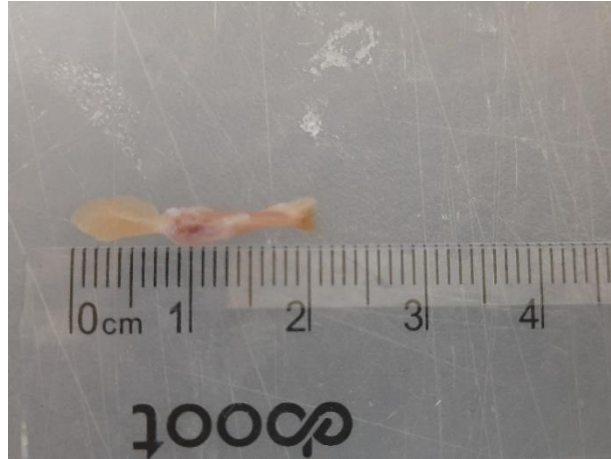


Figure 6: Mouse bone-rotator cuff tendon complex.

- 2) Post defrosting, the thickness and width of the tendon were measured with a digital caliper at multiple locations. The initial gauge length of the tendon after being mounted onto the uniaxial testing clamps was also measured with a digital caliper and noted down for strain calculation.
- 3) The uniaxial machine had a bath chamber filled with phosphate buffered saline (PBS) so that the sample could be immersed in PBS during the mechanical testing.

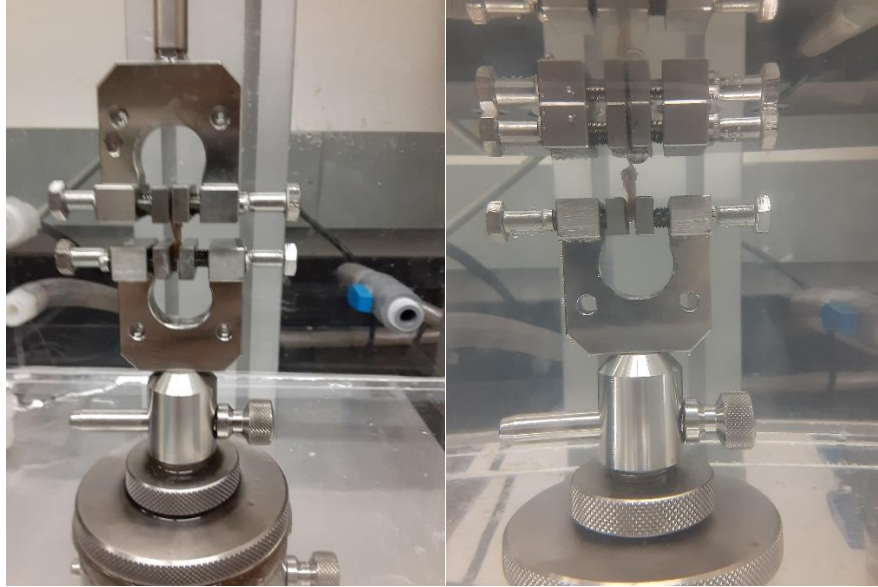


Figure 7: Left – Test-Resources sample clamps. Right – Sample was mounted with two clamps and immersed with PBS in bath chamber.

- 4) Note that an initial trial test failed due to the delicate muscular end of the tendon, which was damaged by clamping pressure. This problem was solved by attaching a small polyethylene polymer strip to the muscular end with minimal amount of superglue. The polymer strip provided the needed reinforcement to avoid clamping damage, as well as prevent slippage of the sample from the clamp at this end. Extreme care was taken to ensure that the superglue was not applied on the tendon so as to preserve its mechanical integrity.

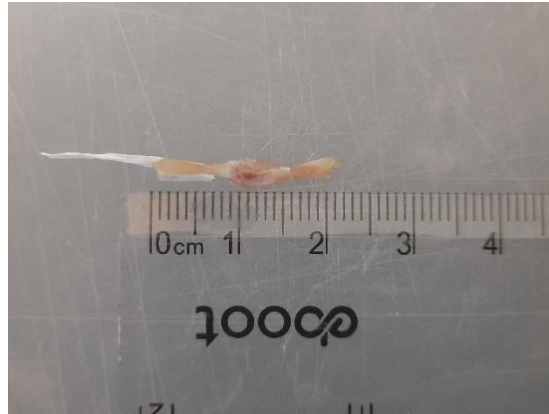


Figure 8: Polyethylene strip was attached to reinforce the muscular end of the tendon.

- 5) After preconditioning, the sample was subjected to tensile load up to failure.
- 6) It is interesting to note that there was not a significant correlation between the size of the samples with respect to age; however, we noticed that the odor emanated from the samples seemed to be particularly strong when samples belonged to old group.
- 7) Once all the data has been collected, they were exported to excel spreadsheets for data analyses,

2.2.2. Data analysis

The following parameter values were calculated

- 1) Convert load from gram to N.
- 2) Calculate the engineering stress by normalizing load to the average cross-sectional area.
- 3) Calculate engineering strain by normalizing the change of displacement (deformation) to the initial gauge length of the tendon.
- 4) Obtain stress-strain curve (will also be used in ANSYS curve fitting)
- 5) Calculate the maximum tensile modulus and read the failure stress and failure strain from the stress-strain curve.

2.2.3. 3D Reconstruction from CT images to obtain 3D model

I) Tendon Model

- 1) Micro CT scans were obtained from UNMC in an image stack of over 1000 images.
- 2) The next step was importing the images in an imaging software and converting the collection into a 3D model; however, the most commonly imported file format that the imaging applications can read is the DICOM format. The dataset obtained was in .BMP, which was not detected by majority of software. and the ones that did succeed in importing an image could only load a single file and not an entire set, which is essential for creation of a 3D model.

An alternate path to creating a model had to be found, the author realized that individually importing files in MIPAV imaging software could facilitate the conversion; however, even after the images set was generated, the software failed to detect that all the images belonged to the same set, and further inspection revealed that every CT scan image set has its own unique timestamp and a serial number that links it to all the other images in the set, which was lost upon conversion, and the only other way of reserializing the set was coding in MATLAB, which would be time consuming and beyond the scope of this project.

- 3) The issue was finally resolved when it was discovered that 3D Slicer, a comprehensive imaging and stl modelling editing software was able to read dataset in .bmp format and generate a 3D model from the set. The functionalities used for modelling are as follows.

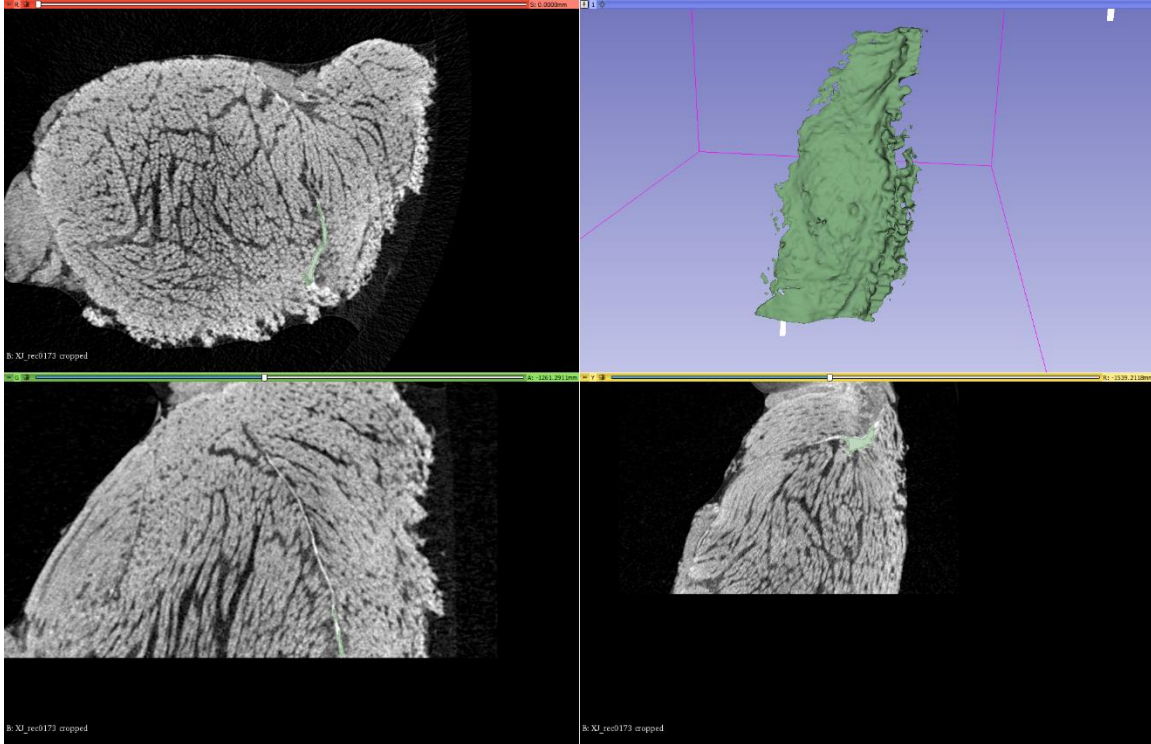


Figure 9: Preview of the reconstructed tendon model using 3D slicer software.

- i. Crop: Due to the large image size, the imported project would be cumbersome with high computing cost and difficult to edit quickly. Crop removed the peripheral image portion and retained only the section with the tendon in it.
- ii. Segmentation module: In order to isolate the region of interest from the scan, a new segment is created to perform the series of operations.
- iii. Threshold tool: This tool is useful when the region of interest has a very high contrast compared to the rest of the scan. As seen in the CT scan image, the tendon is clearly visible, the threshold slider is adjusted depending on the saturation levels of the color so that regions of interest are highlighted. The most ubiquitous setting is selected to provide the most accuracy while generating the 3D model with minimal loss of the object's features.

- iv. Island tool: The connected components in a segment are called islands, one can select the largest island which would guarantee that most of the required region is retained, and the smaller ones are eliminated thereby reducing the noise generated by unwanted speckled regions.
- v. Scissor tool: Segmentation by threshold causes regions with similar intensity to get highlighted, irrespective of their direct relation to the desired feature. This is a problem, as upon converting the CT image to a 3D model, the unrelated bits materialize at random parts and increase the inaccuracy of the model, the scissors tool is an excellent way to get rid of unwanted speckles throughout the image set.
- vi. Smoothing Filters²⁵
 - a. Closing: Closing fills sharp corners and holes smaller than the specified kernel size. Does not remove anything from the segment. Applied to selected segment only, depends on the range of kernel size.
 - b. Median smoothing: Used for intensive smoothing operations, it effectively removes small extrusions and fills small gaps while keeps smooth contours relatively unchanged. Its application is limited to selected segments only.
- vii. The model is finally exported to a new model hierarchy and then saved as a .stl file, which can be further edited in any CAD software.

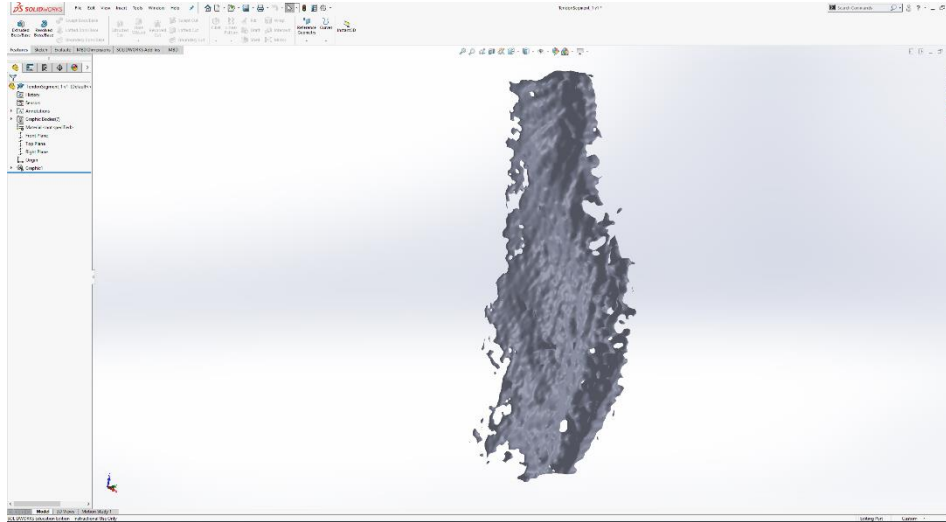


Figure 10: The geometry is imported as a non-editable graphic due to its large size and complexity.

- 4) The original model was too large and complicated to be used for simulation. The .stl model was thus imported in MeshLab, an open-source software, for optimization. The operations conducted in MeshLab are as follows.
 - i. **Remove duplicate face:** This operation eliminates the faces that are defined by the same vertices, because such entities are redundant in defining the overall geometry. If left unchecked, such faces persist in the model. When imported in a CAD analysis software, those duplicates are expressed as a 2D surface attaching to the 3D geometry. This gives erroneous results and could also cause the simulation to crash.
 - ii. **Remove duplicate vertices:** Duplicate vertices are a result of inefficient conversion of one file format into another; It is essential to remove such objects to avoid the possibilities of computational errors during simulations.
 - iii. **Remove zero area face:** These anomalies are a result of three vertices

occupying the same position, creating a non-existent body. The filter removes such vertices, effectively reducing the noise generated by their presence.

- iv. **Remove unreferenced vertices:** These are the vertices that are not assigned to any triangle in the mesh model, only defined purely by their mathematical position in the spatial geometry.
- v. **Quadric edge collapse decimation:** The original .stl file had 319,764 vertices and 639,384 faces. This number is unwieldy and takes up memory space when being imported in any CAD or modelling software, especially in ANSYS for simulation. It is therefore imperative to reduce the total number of faces and vertices of the geometry. After the smoothening and simplifying procedures, the total number was 453 vertices and 913 faces. This enabled the body to be imported into Solidworks as an editable model and not as a view only graphic.
- vi. **Laplacian smoothening/Laplacian smoothening with surface preservation:** The quad collapse decimation results in the object oozing in significant portions due to the loss of triangles. Smoothing is thus done to remove jagged edges, suppress crests, and fill up valleys for a uniform surface finish.
- vii. **Select self-intersecting edges and delete selected edges:** This is a very aggressive approach to removing problematic elements, as they would pose an obstacle when meshing the object for further simulation.
- viii. **Close holes:** This cleaning filter identifies enclosed cavities that are lacking a single surface holes, which are “small” with respect to the mesh size, possibly almost planar³⁴

Simple filter: Remeshing → simplification and reconstruction → Close Holes.

- ix. **Summary:** The object being complicated in its topography, needed several iterations of QC decimation, Laplacian smoothening, select and delete self-intersecting surfaces, and fill holes in succession. the ideal model, free of defects and unnecessary noise, was obtained from trial and error, it is depicted below.

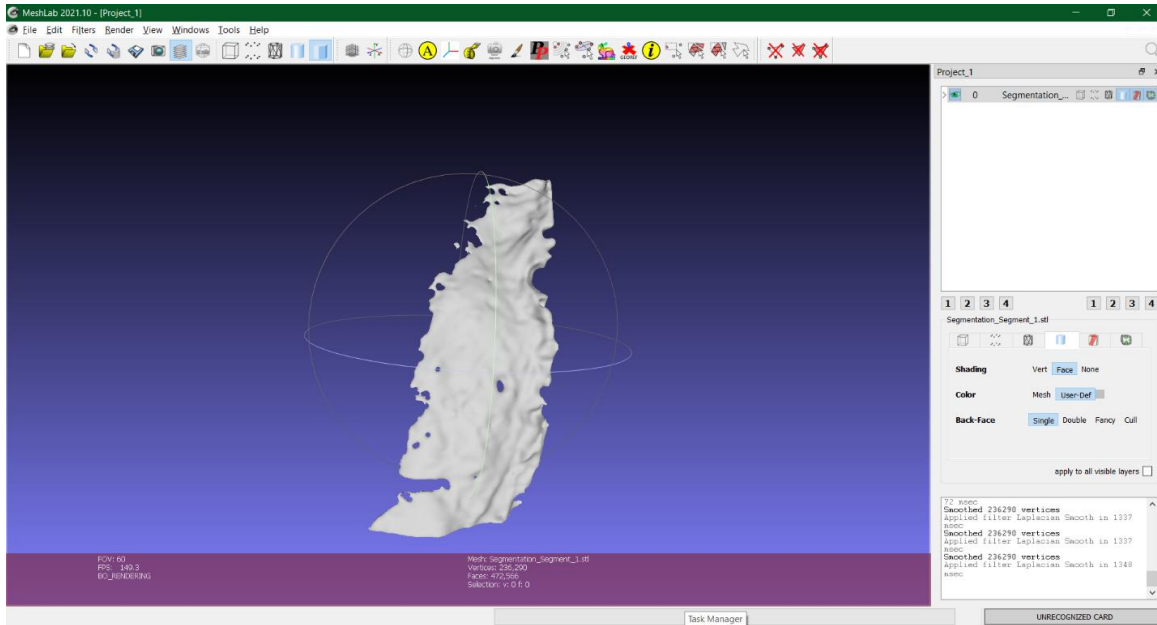


Figure 11: Before Laplacian smoothening.

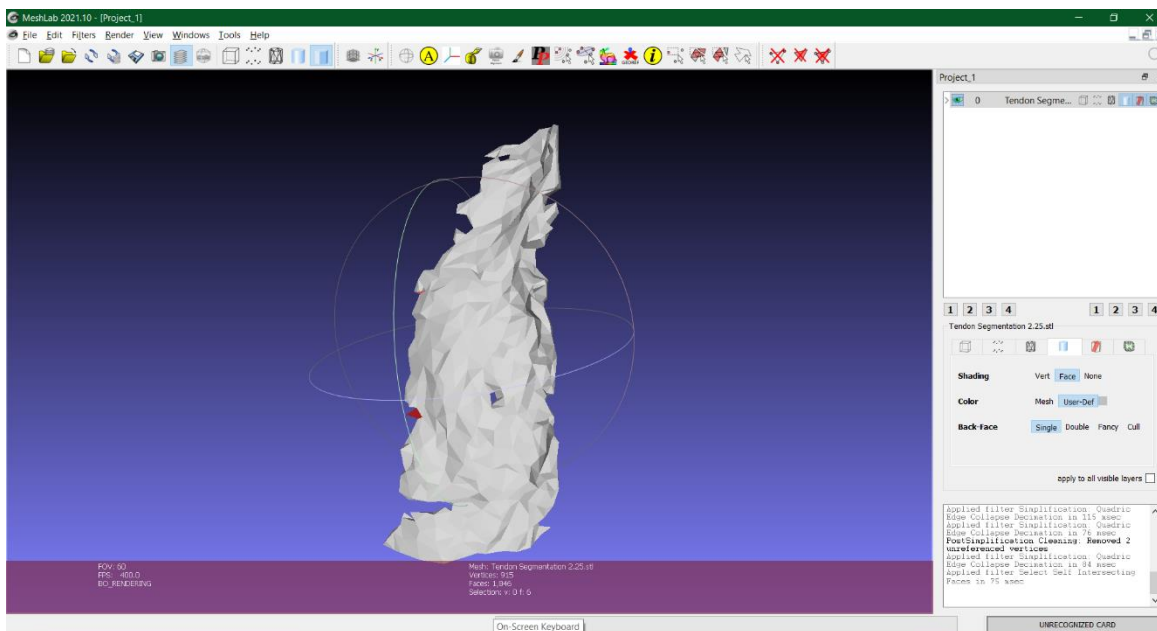


Figure 12: After Laplacian smoothening with self-intersecting face selected.

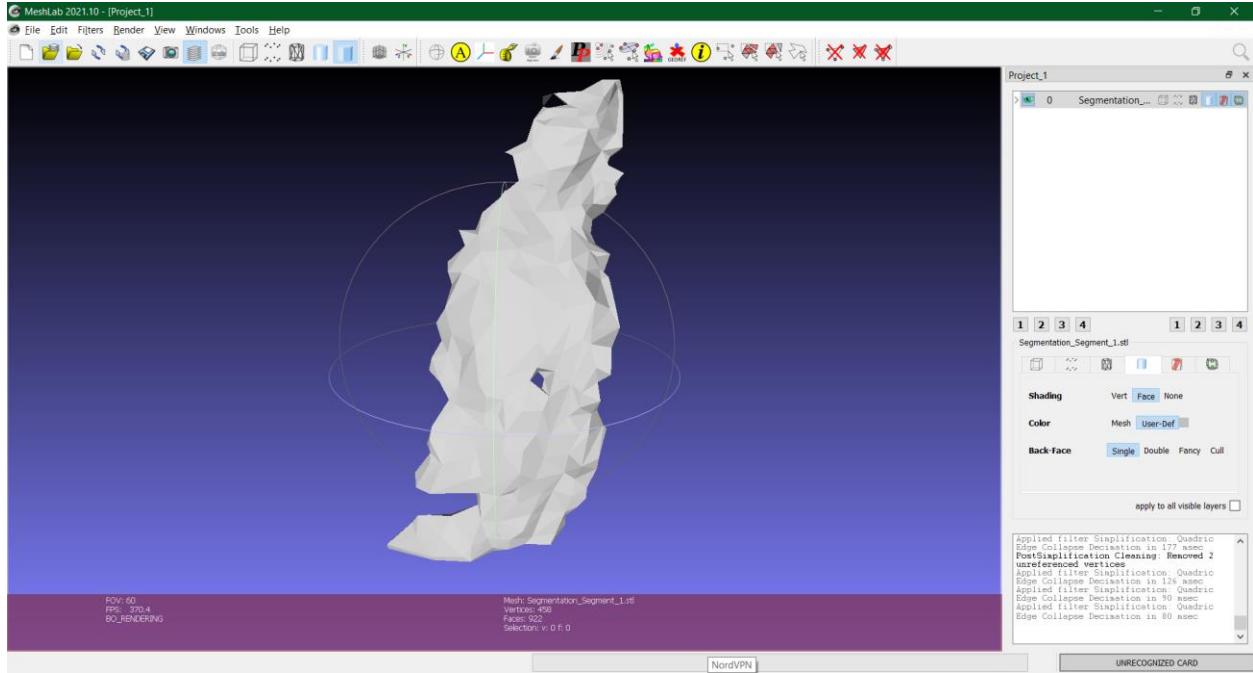


Figure 13: After quadratic edge collapse decimation.

- 5) **Post processing:** After the finished tendon model was obtained, certain discrepancy was noticed in not just the size but also the geometrical feature between the 3D model and the actual specimen.

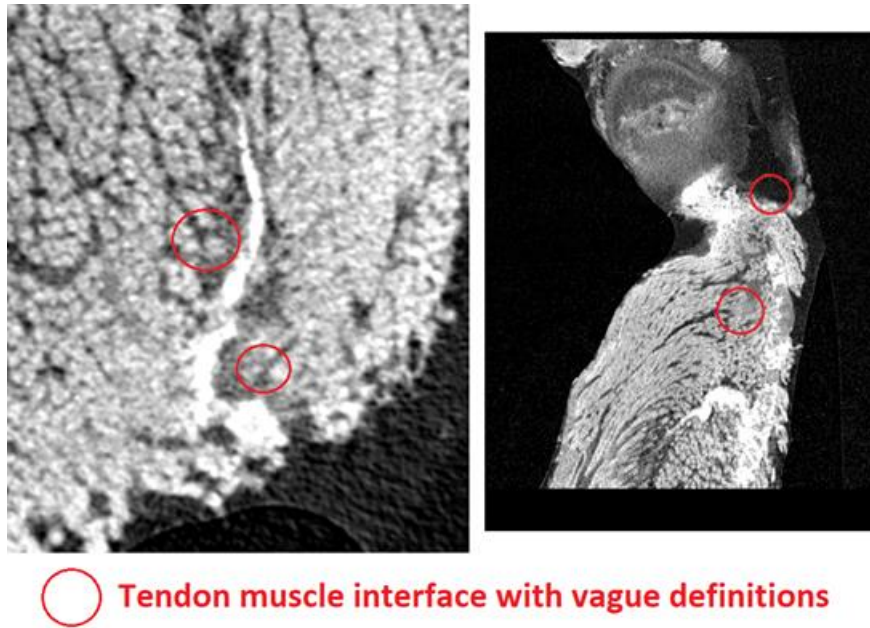


Figure 14: The anatomy of tendon-muscle interface shown by Micro-CT image.

To clarify these rising doubts, personnel who had worked on the mouse tendon harvesting and sample preparation were contacted. It was revealed that, after the sample is harvested, the connective tissue surrounding the tendon is removed for a cleaner sample, which would be better suited to mechanical testing and would provide an accurate assessment of the tendon mechanical properties. The scans, on the other hand, were not from any of the samples that were tested but from intact animal shoulder. Since the tendon is embedded in the muscle, the feature of tendon (bright white contrast) is quite fuzzy around its boundary.

The above revelation explained the unnecessarily complicated geometry of the 3D model. To rectify this mistake, the image data set was resampled, and a ‘mold’ was generated, which would be used to trim the final model. The dimensions of the mold

were obtained by scaling the CAD geometry with the average length of the samples belonging to the same age group. Eventually the mold's dimensions were imported in solid works, where the tendon sample was trimmed down to only its essential shape by extrude cut function. The comparison before and after trimming is depicted below.

It is important to note that the anatomically accurate 3D model is required for simulation in ANSYS, and the first purpose of the simulation is to be able to corroborate the results obtained in our mechanical testing. After the above processing, we confirmed that the model bears a resemblance to actual specimen geometry, and the model generated from the CT scans is not scaled up or down and can be used for simulation.

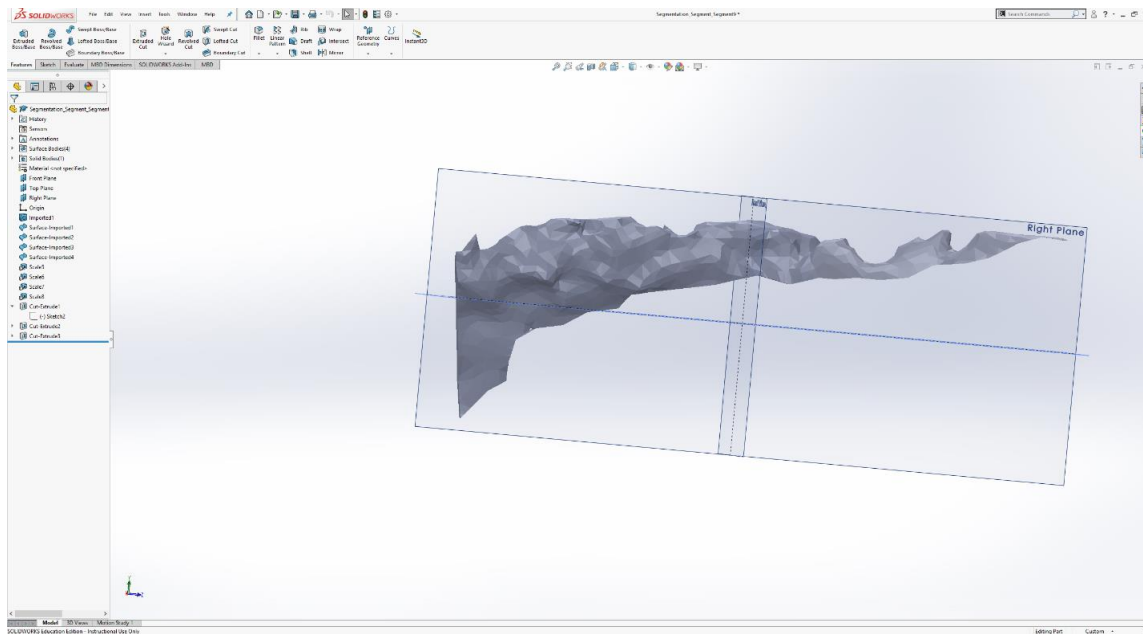


Figure 15: Tendon imported as a non-editable graphic due to extreme complexity.

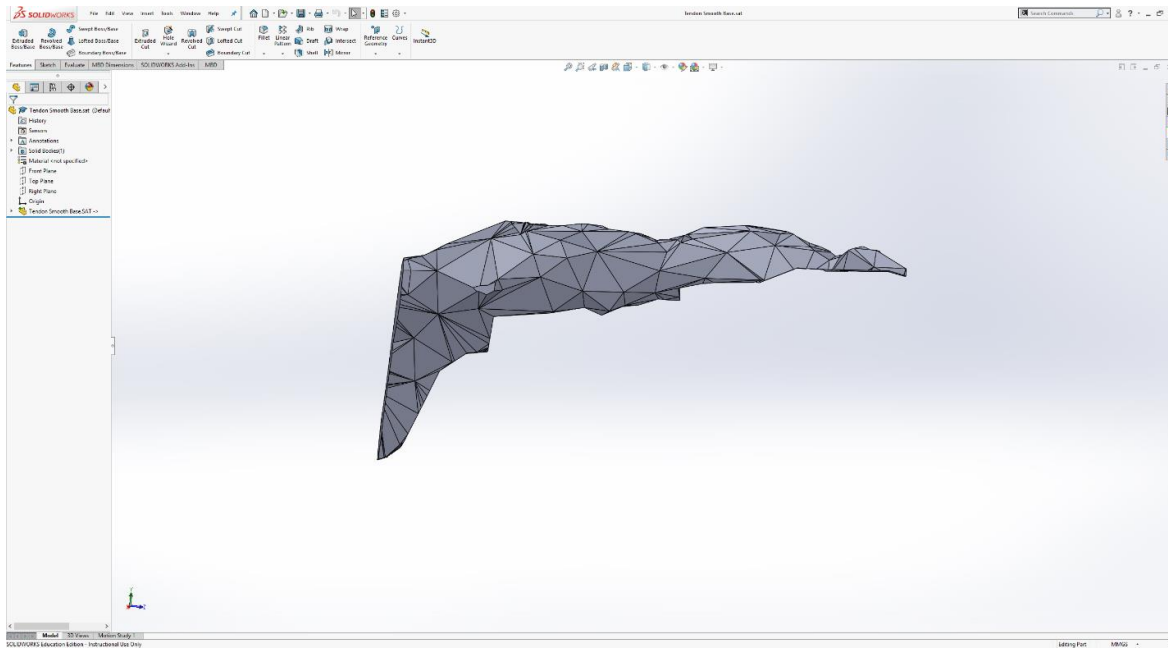


Figure 16: Simplified tendon model.

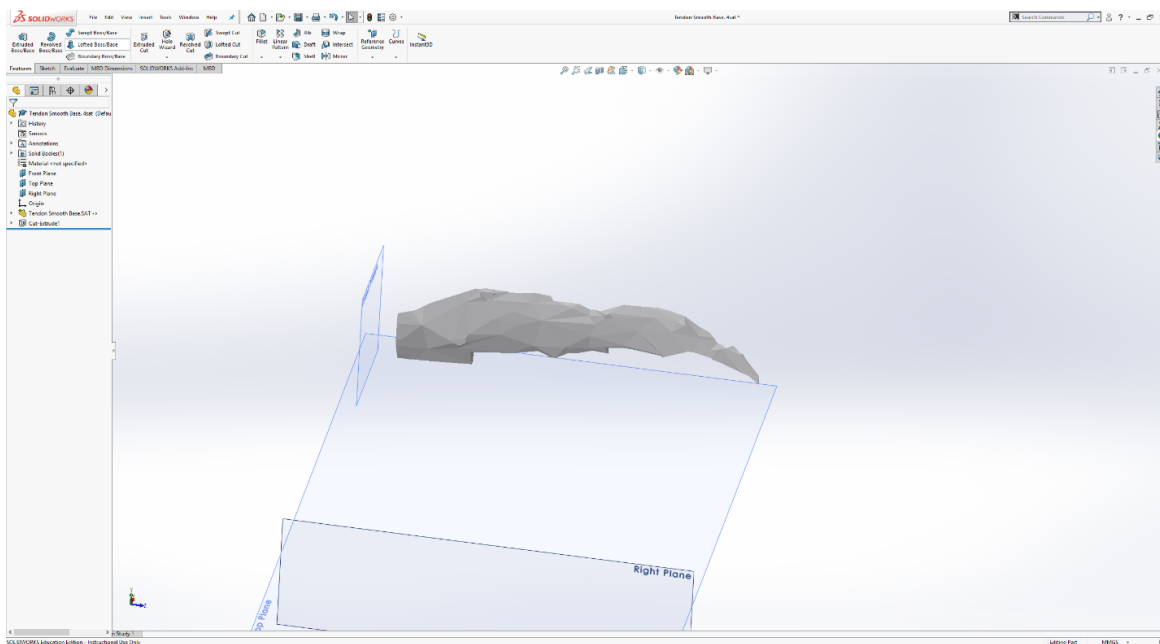


Figure 17: Final simplification in MeshLab.

II) Bone Model: The CT scan image set for shoulder bone was acquired from UNMC in DICOM format, which made it easier to convert the data set to a 3D model.

1) **MITK software:** The CT scan images were imported in MITK software, and the operations conducted are as follows.

- i. **Crop using bounding box:** There was a lot of unwanted information, such as peripheral muscle tissues. In order to create a focused model, a bounding box is created around the desired features to isolate the area of interest by removing unnecessary background.
- ii. **Segmentation:** After thresholding, a 3D model of the bone was created.
- iii. **Add/Subtract/Fill tools:** Due to the low resolution of the CT images, every slice had to be individually analyzed, and some relevant portions of the images were manually corrected. Once an image with a closed boundary was obtained, it was uniformly filled.
- iv. **Volume rendering:** A 3D polygon is generated from the segmented area and saved as a printable .stl file.

However, as depicted below the model generated is a hollow object, bound by surface geometries with no thickness. To create a solid body from the surface model, it was exported to Solidworks and auto desk for repairing and modifications. The steps were described as follows.

2) Autodesk

- i) **Surface create:** Two reference planes were created as boundaries for the tendon bone piece as the base and the top, and surface generating feature was employed to fill the hollow geometry with triangular tessellation to

create a solid geometry.

- ii) **Stitching:** The open surfaces that need to be stitched together are selected. Then, depending on the specified tolerance, the operation is carried out. The tolerance controls the proximity of the edges of the surfaces, which needs to be validated so that the two surfaces can be stitched together. For stitching wider gaps, the tolerance needs to be increased.
- iii) **Prerequisite Checker:** An invaluable tool in Autodesk that enabled the miniscule errors and un-joined edges in the model to be detected and fixed. This was a crucial step in generation of anatomical relevant 3D bone model.

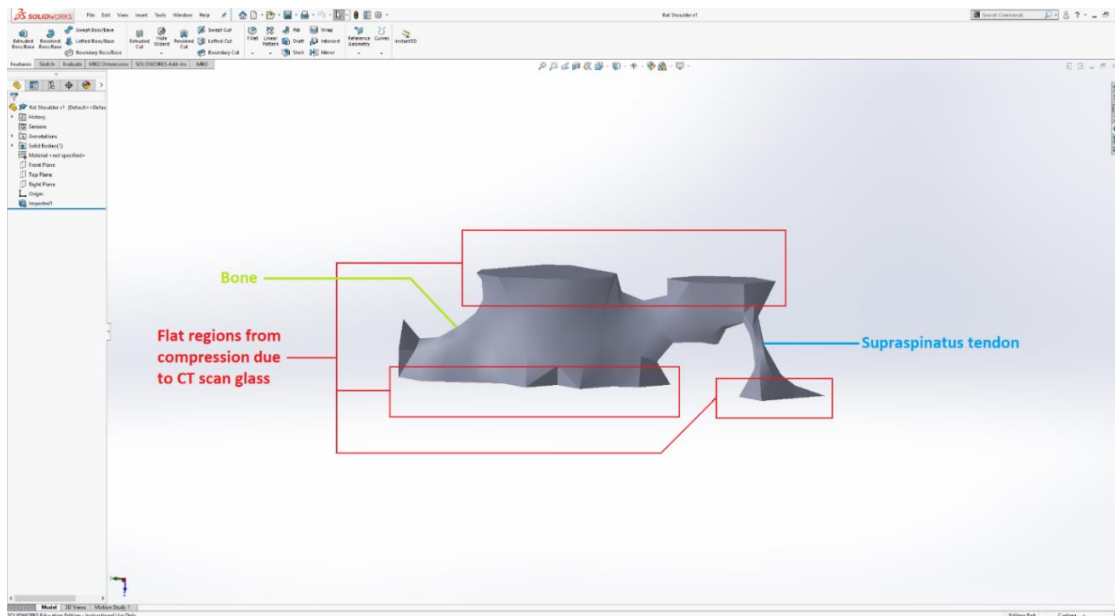


Figure 18: Default geometry of the bone after reconstruction.

3) Solidworks

- i) **Import:** This might not seem like an important operation to be performed by the user; however, the importing parameters and conditions played an extremely important role in this project. While importing a new geometry,

upon clicking the options tab, one can select whether the solid needs to be imported as a solid body, surface, or a mesh, the option of solid body must be chosen.

- ii) **Repair:** The imported body is defective, with redundant faces, unallocated vertices, self-intersecting planes etc. Most CAD software possess a repair function, which checks the object on import and removes the defects by filling minor cracks, generating surfaces to bridge crevices, remeshing the object to account for loss of tessellation, endemic to frequent changes in file format extension.

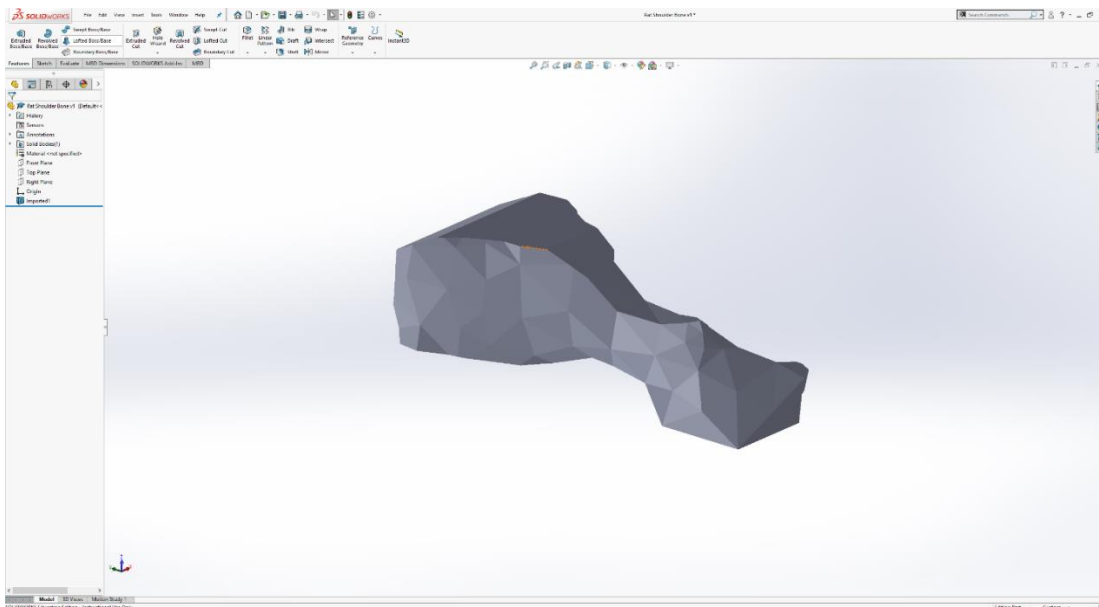


Figure 19: Bone geometry with unnecessary parts removed.

- iii) **Aesthetic modification:** The CT scan images were not very detailed and the resulting model did not achieve satisfied resemblance to the actual bone anatomy. Common CAD modelling functions in Solidworks and Autodesk fusion 360 were used to bring the likeness of the 3D model as close to the

actual bone as possible. The finished model is depicted below

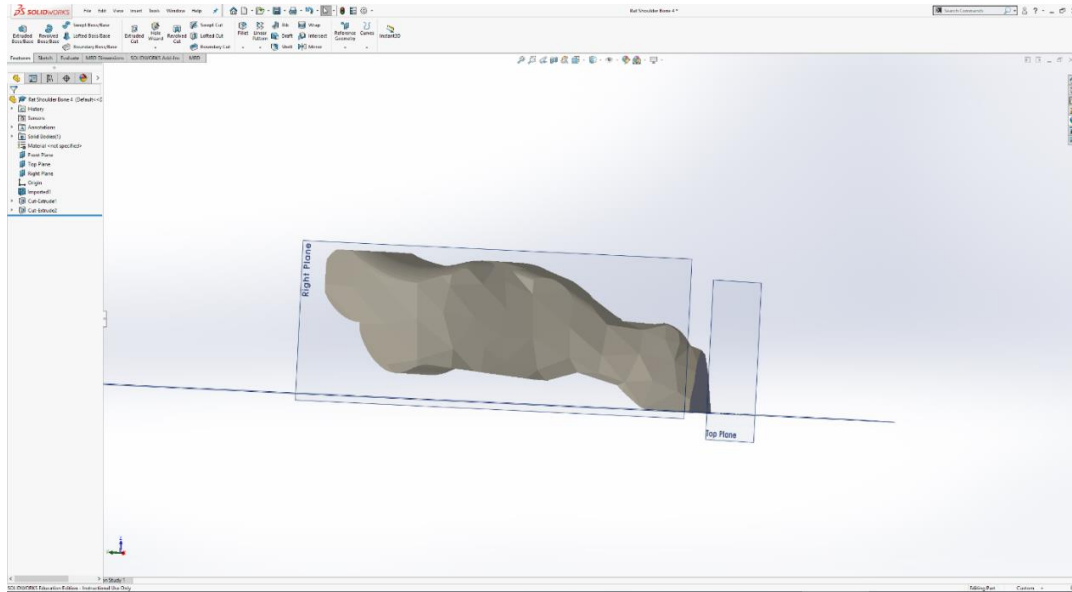


Figure 20-A: Final bone model.



Figure 20-B: Actual bone for comparison.

iii) **Mating:** The two components were now fully formed, and free of any defect.

The bone and tendon were mated as an assembly in Solidworks.

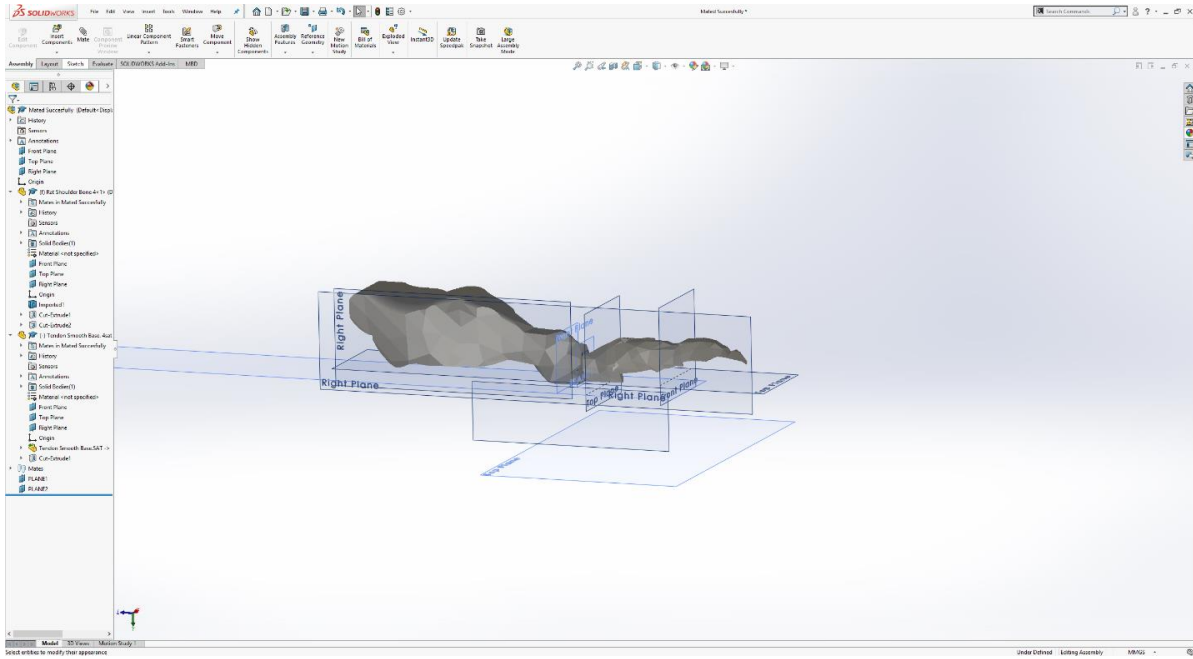


Figure 21-A: Bone-tendon integrated model.

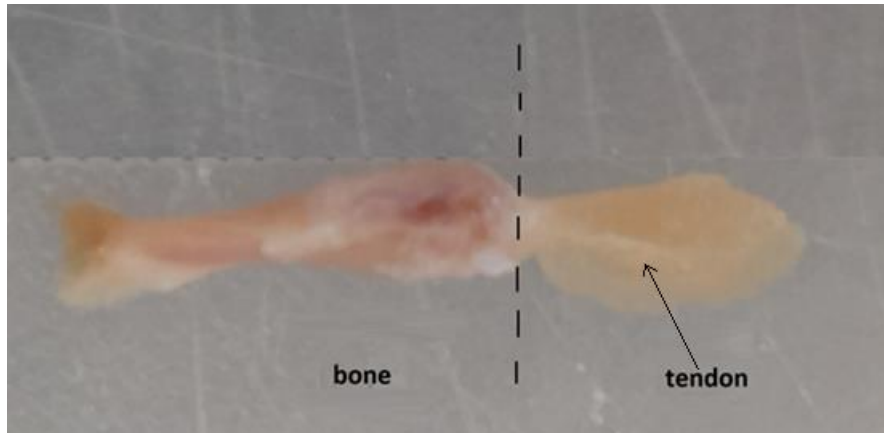


Figure 21-B: Bone-tendon sample for comparison.

2.2.4 FEA simulation: Now that the model to be tested has been finalized, and data from actual uniaxial tensile testing has been obtained, we were able to perform FE simulation.

The ANSYS modeling and simulation protocol is described as follows.

- i) **Engineering Data:** The material properties of each group were assigned to each simulation. The stress-strain curve of each group was fed to produce the coefficients of the Mooney-Rivlin model. Material properties of bone was also assigned.
- ii) **Geometry:** The design modeler in ANSYS was used to import the 3D model of the bone-tendon complex.

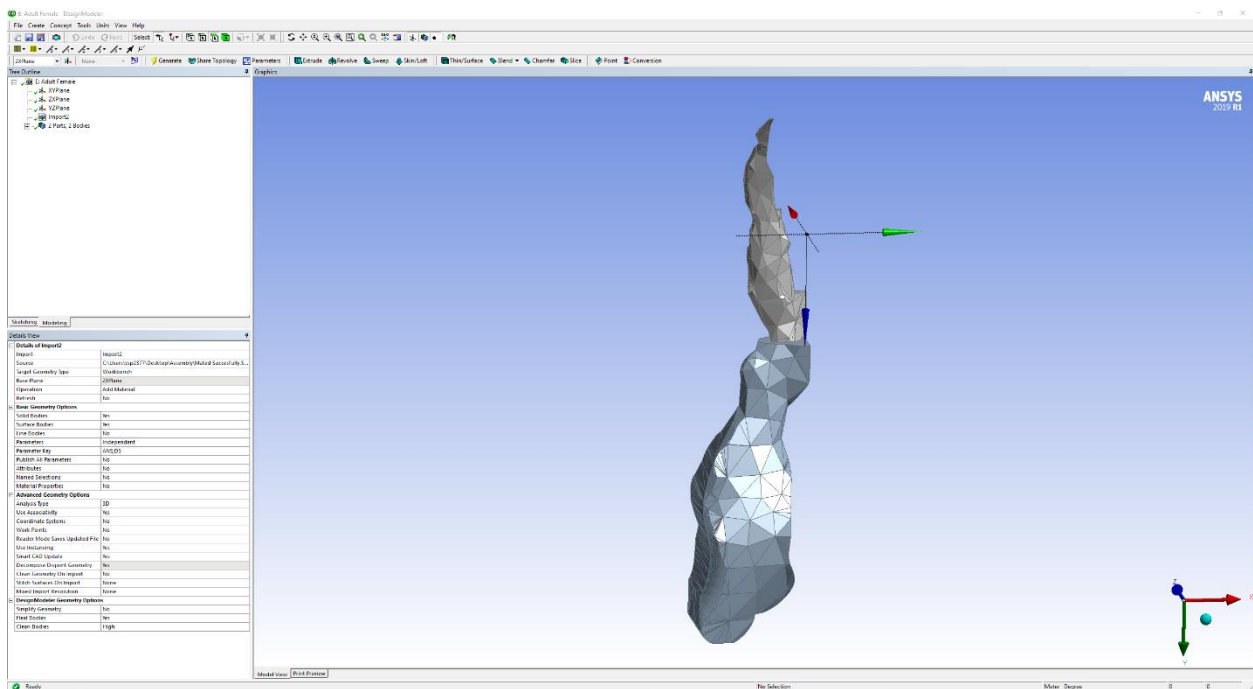


Figure 22: Tendon-Bone geometry imported in ANSYS design modeler workspace.

- iii) **Model meshing:** Meshing were performed after the imported model is assigned material properties. The sizing was chosen as 5 (on a scale of 0-7, 7 being the finest) based on our mesh convergence result.

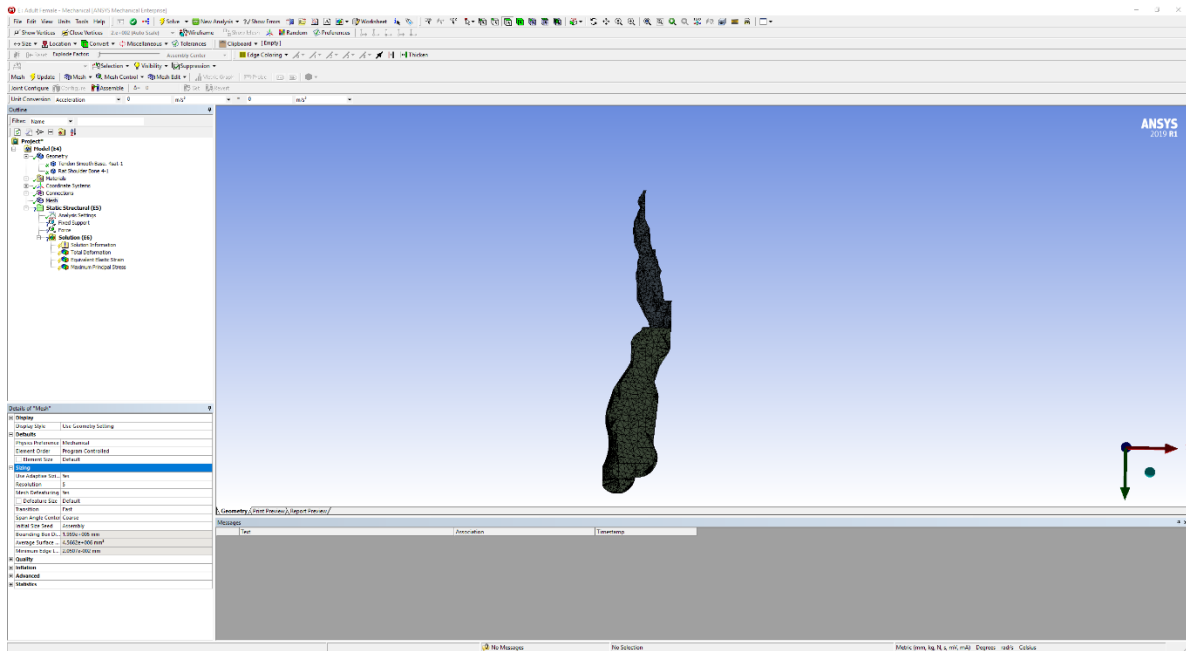


Figure 23: Tendon model after meshing is complete.

- iv) **Boundary condition and load application:** The bone-tendon interface was set as fixed support. Force was applied at the free end of the tendon. The setup is meant to mimic actual experimental setup. The tip of the tendon is subjected to 0.5 N force.

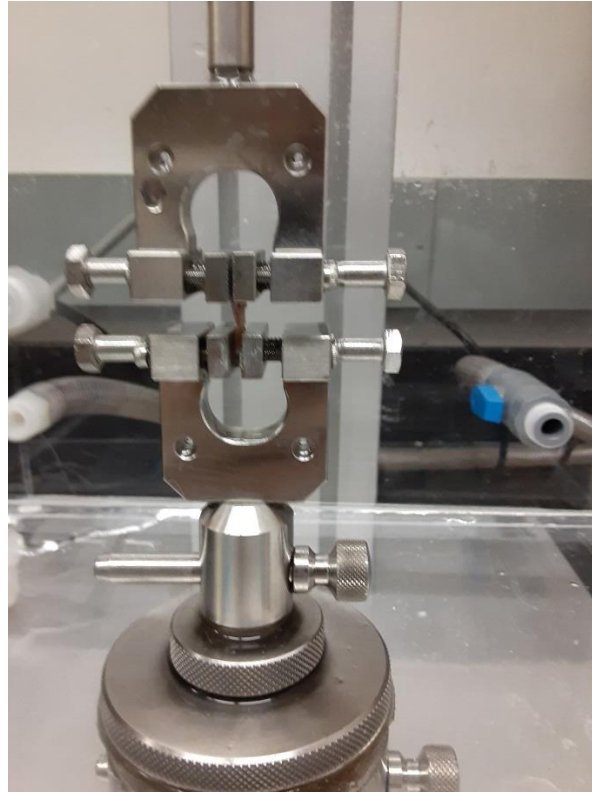


Figure 24: The bone-rotator cuff tendon complex under uniaxial tensile mechanical testing.

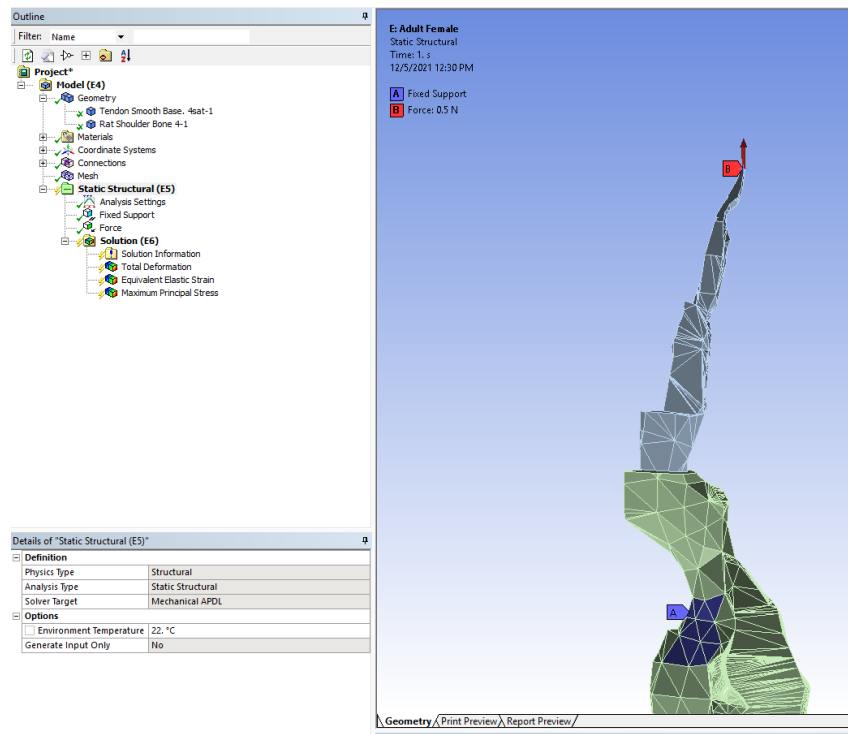


Figure 25: Comparison of actual test setup and virtual simulation. the red arrow on top depicts 0.5 N force, the purple region on the bone segment is fixed support intended to mimic the clamp.

- v) **Analysis settings:** large deflection has been switched on because hyperelastic materials undergo large deformation. In order to compute and view the results it is necessary to enable this option.

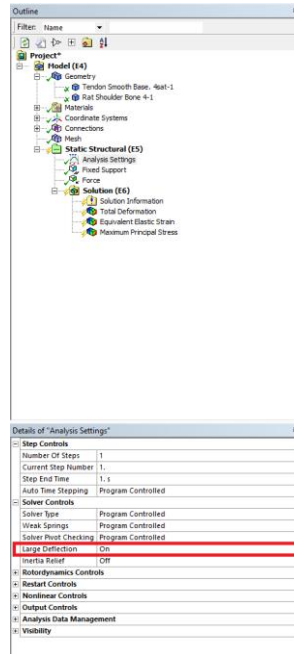


Figure 26: ANSYS workbench setting for simulation.

Chapter 3: RESULTS AND DISCUSSION

3.1 Mechanical testing results.

The failure stress-strain curves of the bone-rotator cuff complex are depicted below. The failure stress, failure strain, and maximum tensile modulus were obtained from the stress-strain curves. Maximum tensile modulus was calculated by linearly fitting the curve before the yielding point. The overall trends among young, adult, and old groups, as well as female versus male, are also tabulated below.

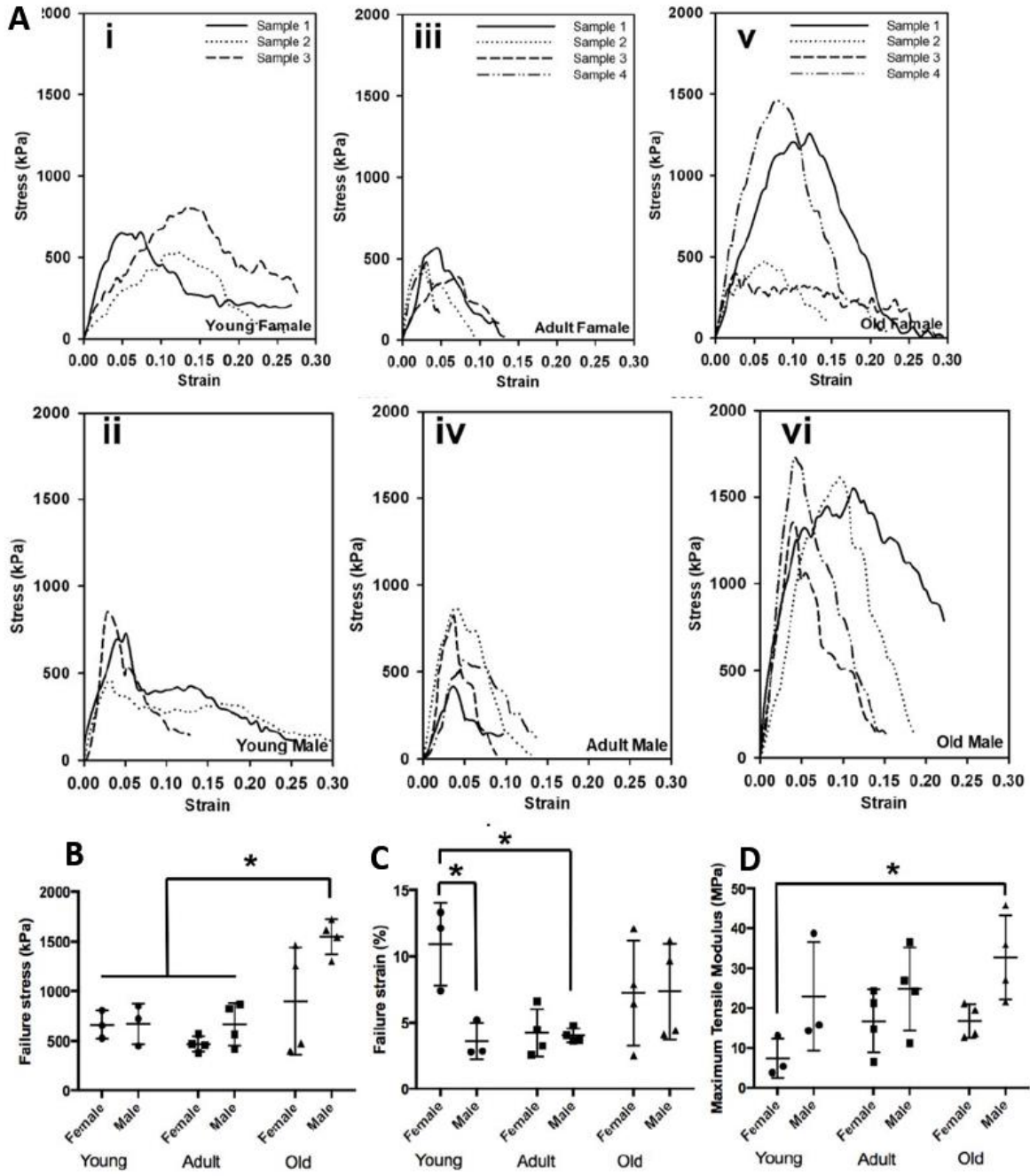


Figure 27: (A) Failure stress-strain curves for (i) young female group, (ii) adult female group, (iii) old female group, (iv) young male group, (v) adult male group, and (vi) old male group. Comparisons of (B) failure stresses, (C) failure strains, and (D) maximum tensile moduli among the young female, young male, adult female, adult male, old female, and old male groups.

Table 2: Failure stress of the bone-rotator cuff tendon complex.

	Female (kPa)	Male (kPa)
Young	662.83 ± 115.14	673.34 ± 167.22
Adult	468.59 ± 67.52	668.74 ± 184.74
Old	899.05 ± 467.39	1548.50 ± 153.68

Table 3: Failure strain of the bone-rotator cuff tendon complex.

	Female (%)	Male (%)
Young	10.95 ± 2.55	3.62 ± 1.12
Adult	4.23 ± 1.54	4.04 ± 0.44
Old	7.25 ± 3.42	7.35 ± 3.14

Table 4: Maximum tensile modulus of the bone-rotator cuff tendon complex.

	Female (MPa)	Male (MPa)
Young	7.41 ± 4.04	22.95 ± 11.16
Adult	16.75 ± 6.83	24.76 ± 9.05
Old	16.80 ± 3.68	32.71 ± 9.13

An increasing trend was observed from young, to adult, to old mice, but only the difference between old male and young female groups was significant. There was no observable trend in the failure strain, except the complexes of young females had larger failure strains (more extensible) compared with the young male and adult male groups. The male mice had higher overall failure stresses than the female mice in adult and old groups, and the male mice had

larger overall maximum tensile moduli than the female mice in all three age groups.

3.2 ANSYS simulation results

We have successfully established the FE model for mouse bone-rotator cuff tendon complex and performed computational simulation using ANSYS workbench. The plots for von Mises stress generated from FE simulations were presented in following Figures. The trend that predicted from in FEA analysis is consistent with the overall trend observed from the uniaxial mechanical tests.

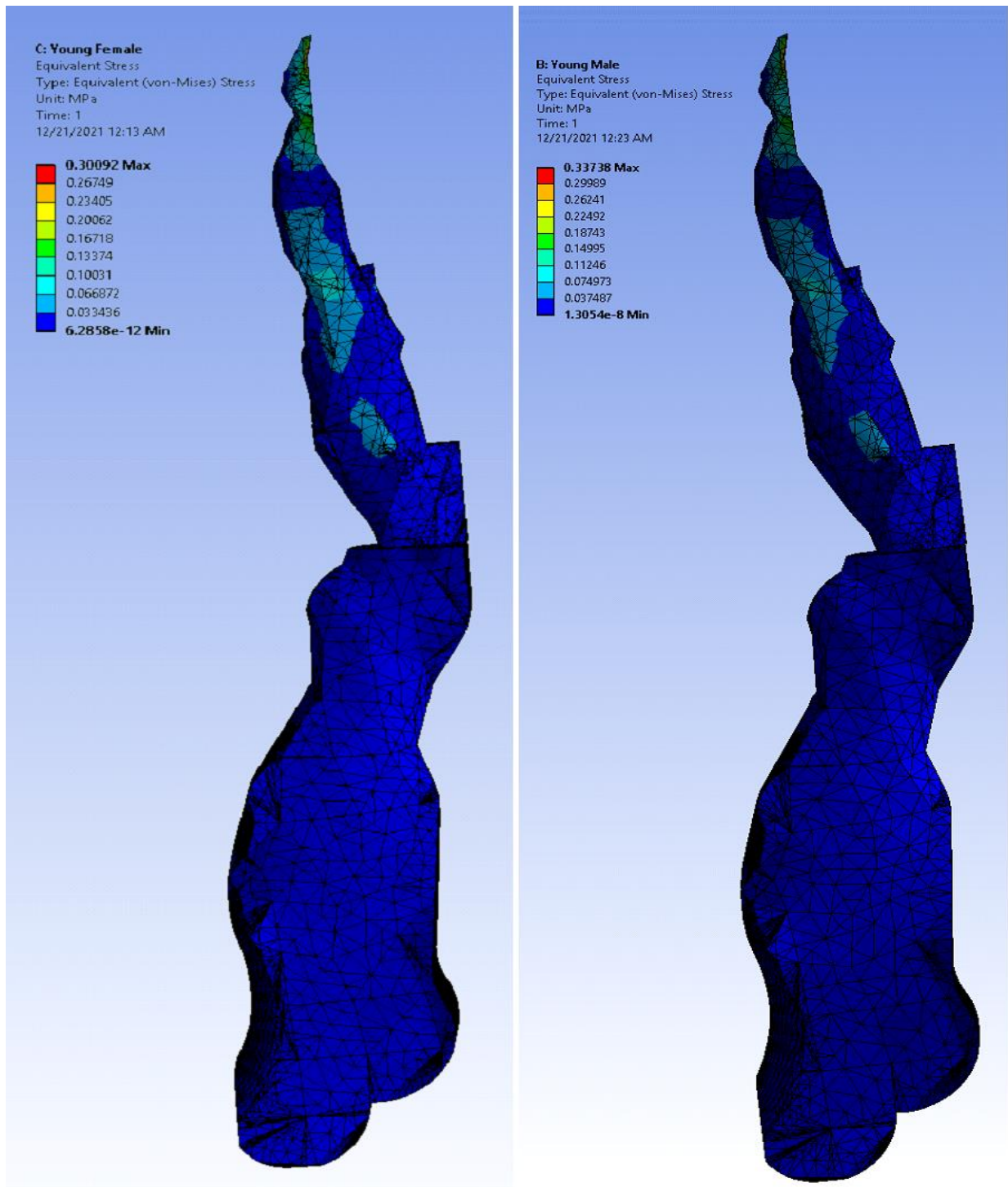


Figure 28: Von Mises stress plot generated from FE simulation of the bone-rotator cuff tendon complex of young male and female mice.

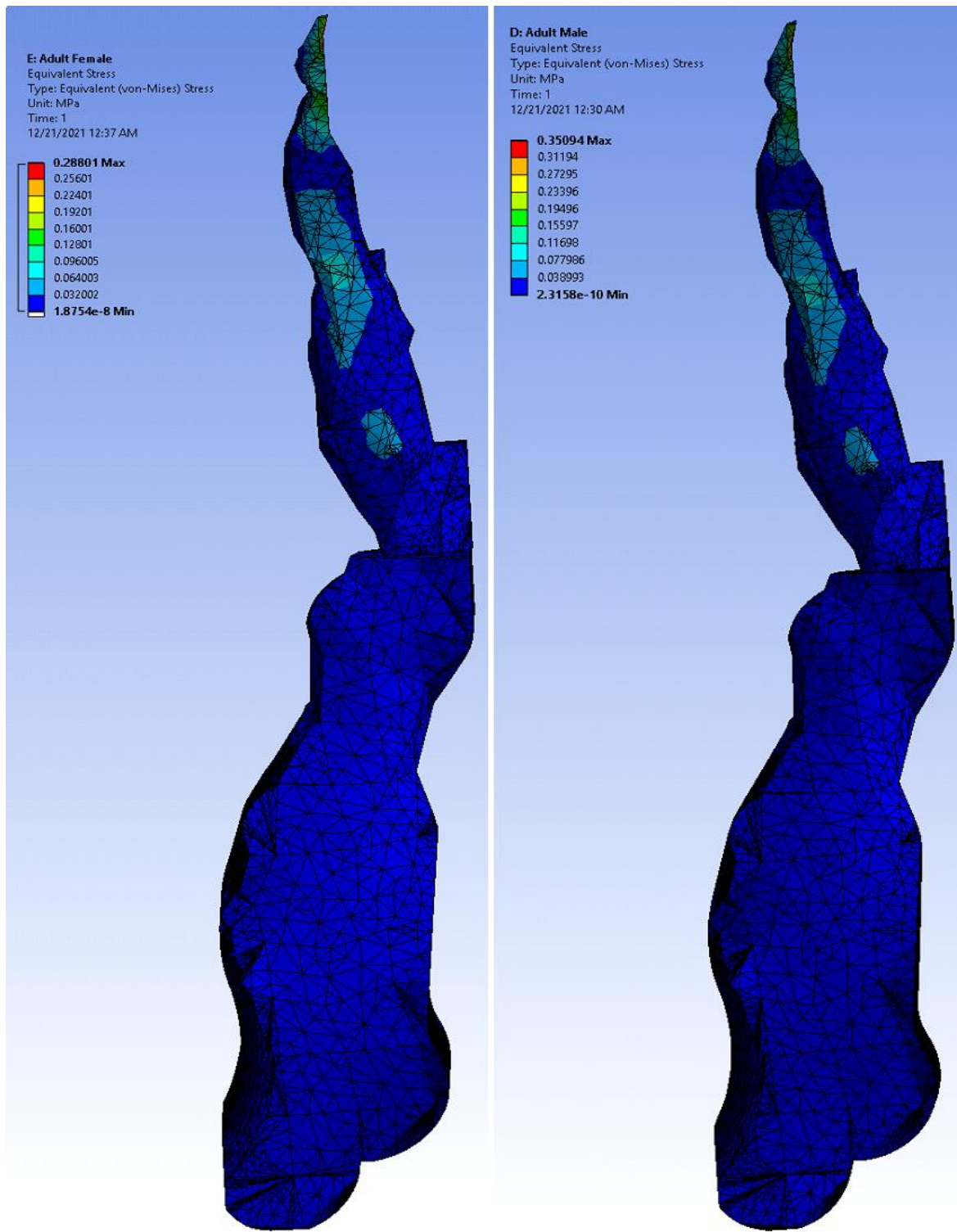


Figure 29: Von Mises stress plot generated from FE simulation of the bone-rotator cuff tendon complex of adult male and female mice.

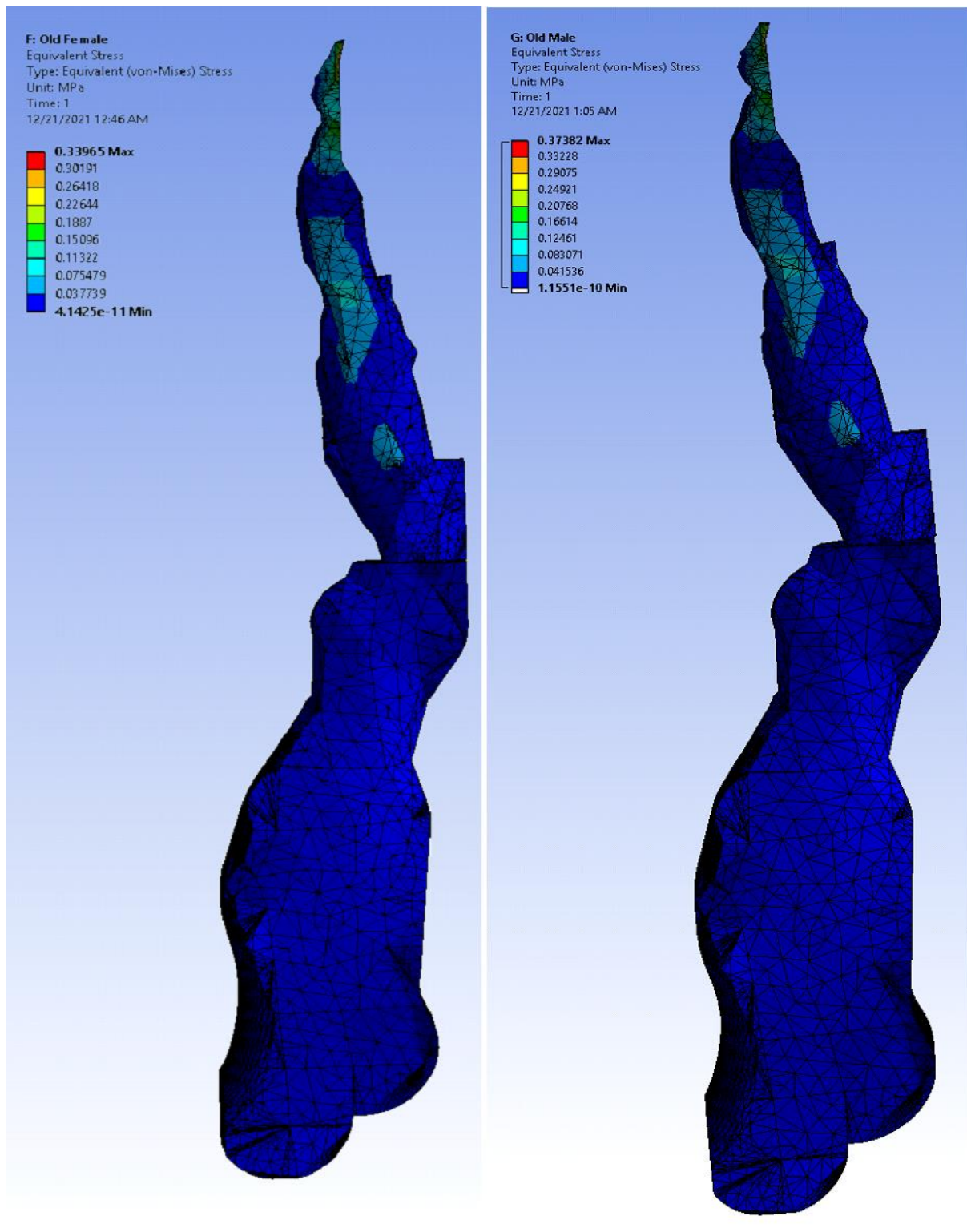


Figure 30: Von Mises stress plot generated from FE simulation of the bone-rotator cuff tendon complex of old male and female mice.

3.3 Limitations and further improvements

Despite the successful establishment of mechanical testing, 3D reconstruction, and FE modeling and simulation protocols and having obtained the desired results, the project can be further improved in the future by addressing some limitations.

- 1) Although with high resolution, the micro-CT scan of tendon still had noises causing the unevenness of the reconstructed 3D model. In the future, micro-CT protocol can be improved to improve the tendon imaging to achieve high quality 3D reconstruction. This will reduce the need for geometrical smoothing, simplification, and optimization, which might cause loss in anatomical details.
- 2) Hyperelastic model was used for the current study. Future study can include stress relaxation testing and model the tendon as a viscoelastic material.
- 3) The major focus of the collaborative project conducted in UNMC was the study of tendon-bone interface. The first set of micro-CT images on both bone and tendon had a very poor resolution. The second micro-CT dataset, despite with high resolution and many anatomical details, only depicted the tendon and not the site of enthesis. Having a micro-CT dataset with the tendon-bone enthesis junction more clearly defined might provide information about enthesis interface and enrich the modeling and simulation efforts.

3.4 Conclusion

- 1) we have assessed the biomechanical properties of bone-rotator cuff tendon complex of male mice and female mice among various age groups (young: 2-3 months old, adult: 6-8 months old, and old: 15-18 months old). The failure stress, failure strain, and maximum tensile modulus were compared to reveal the overall trends among young, adult, and old groups, as well as female versus male.
- 2) We found that, for failure stress (mechanical strength), no difference between young and adult mice was found, while old mice showed increased failure stress, especially the old male mice. The maximum tensile modulus represents the stiffness of the complex. An increasing trend was observed from young, to adult, to old mice, but only the difference between old male and young female groups was significant. No obvious trend exists in the failure strain, except the complexes of young females had larger failure strains (more extensible) compared with the young male and adult male groups. Lastly, the male mice had higher overall failure stress than the female mice in adult and old groups, and the male mice had larger overall maximum tensile moduli than the female mice in all three age groups.
- 3) Our mechanical data showed an interesting observation. The failure stress in the old group, especially the old male group, increased significantly compared to the young and adult groups. The maximum tensile modulus also showed an increasing trend from the young to old groups. Our observation in the mouse model indicates that age alone might not be the dominant risk factor to predict rotator cuff injury rate, and other factors associated with the aging process, like overuse, accumulated tissue damages/injuries, and underlying chronic disease, might contribute to the vulnerability of the rotator cuff in the elderly populations.

- 4) We further performed Micro-CT imaging on the bone- tendon complex and reconstructed its 3D geometrical model using MITK, Slicer, and MeshLab software. With the material parameters obtained from the biomechanical tests, we successful established a Finite Element Analysis model for the bone-rotator cuff tendon complex using ANSYS software and were able to simulate and demonstrate its age dependent mechanical behavior.

References

-
- ¹ The effects of maturation and aging on the rotator cuff tendon-to-bone interface
DOI: <https://doi.org/10.1096/fj.202101484R>
- ² Numerical thermal simulation of cryo-exposure using Ansys January 2020MATEC Web of Conferences 324:01002 DOI: 10.1051/mateconf/202032401002
- ³ A method to test contractility of the supraspinatus muscle in mouse, rat, and rabbit Ana P. Valencia, Shama R. Iyer, Stephen J. P. Pratt, Mohit N. Gilotra, and Richard M. Lovering 01 Feb 2016 <https://doi.org/10.1152/jappphysiol.00788.2015>
- ⁴ Humeral Insertion of the Supraspinatus and Infraspinatus New Anatomical Findings Regarding the Footprint of the Rotator Cuff By Tomoyuki Mochizuki, MD, Hiroyuki Sugaya, MD, Mari Uomizu, MD, Kazuhiko Maeda, MD, Keisuke Matsuki, MD, Ichiro Sekiya, MD, Takeshi Muneta, MD, and Keiichi Akita, MD Investigation performed at the Unit of Clinical Anatomy, Graduate School, Tokyo Medical and Dental University, Tokyo, Japan
- ⁵ https://www.physio-pedia.com/Rotator_Cuff
- ⁶ K. Yamaguchi, K. Ditsios, W.D. Middleton, C.F. Hildebolt, L.M. Galatz, S.A. Teefey, The demographic and morphological features of rotator cuff disease. A comparison of asymptomatic and symptomatic shoulders, *J Bone Joint Surg Am* 88(8) (2006) 1699-704
- ⁷ L.S. Oh, B.R. Wolf, M.P. Hall, B.A. Levy, R.G. Marx, Indications for rotator cuff repair: a systematic review, *Clinical Orthopaedics and Related Research* 455 (2007) 52-63.
- ⁸ D.A. van der Windt, B.W. Koes, B.A. de Jong, L.M. Bouter, Shoulder disorders in general practice: incidence, patient characteristics, and management, *Annals of Rheumatic Diseases* 54(12) (1995) 959-64.
- ⁹ C. Milgrom, M. Schaffler, S. Gilbert, M. van Holsbeeck, Rotator-cuff changes in asymptomatic adults. The effect of age, hand dominance and gender, *J Bone Joint Surg Br* 77(2) (1995) 296-8.
- ¹⁰ T. Teunis, B. Lubberts, B.T. Reilly, D. Ring, A systematic review and pooled analysis of the prevalence of rotator cuff disease with increasing age, *Journal of Shoulder and Elbow Surgery* 23(12) (2014) 1913-1921.
- ¹¹ G. Diebold, P. Lam, J. Walton, G.A. Murrell, Relationship between age and rotator cuff retear: a study of 1,600 consecutive rotator cuff repairs, *The Journal of Bone and Joint Surgery* 99(14) (2017) 1198-1205.
- ¹² Y.S. Lee, J.Y. Jeong, C.D. Park, S.G. Kang, J.C. Yoo, Evaluation of the Risk Factors for a Rotator Cuff Retear After Repair Surgery, *The American Journal of Sports Medicine* 45(8) (2017) 1755-1761

-
- ¹³ Fung YC. “Biomechanics: Mechanical properties of living tissues”, Springer-Verlag, New York, 1993: 242-320.
- ¹⁴ Zeng YJ, Liu YH, Xu CQ, Xu XH, Xu H, Sun GC. “Biomechanical properties of skin in vitro for different expansion methods”, Clin Biomech., 2004; 19: 853-857
- ¹⁵ Lewis JS. Rotator cuff tendinopathy. Br J Sports Med. 2009 Apr;43(4):236-41. doi: 10.1136/bjsm.2008.052175. Epub 2008 Sep 18. PMID: 18801774.
- ¹⁶ Thorpe CT, Screen HR. Tendon Structure and Composition. Adv Exp Med Biol. 2016;920:3-10. doi: 10.1007/978-3-319-33943-6_1. PMID: 27535244.
- ¹⁷ López-Campos JA, Ferreira JPS, Segade A, Fernández JR, Natal RM. Characterization of hyperelastic and damage behavior of tendons. Comput Methods Biomech Biomed Engine. 2020 May;23(6):213-223. doi: 10.1080/10255842.2019.1710742. Epub 2020 Jan 20. PMID: 31958016.
- ¹⁸ Nonlinear Solid Mechanics for Finite Element Analysis: Statics, pp. 158 - 187 DOI: <https://doi.org/10.1017/CBO9781316336144.007>[Opens in a new window] Publisher: Cambridge University Press Print publication year: 2016
- ¹⁹ https://en.wikipedia.org/wiki/Hyperelastic_material
- ²⁰ <https://classes.engineering.wustl.edu/2009/spring/mase5513/abaqus/docs/v6.6/books/gsx/default.htm?startat=ch05s04.html>
- ²¹ <https://en.wikipedia.org/wiki/File:Hyperelastic.svg>
- ²² https://slicer.readthedocs.io/en/latest/user_guide/image_segmentation.html
- ²³ <https://en.wikipedia.org/wiki/Smoothing>
- ²⁴ <http://paulbourke.net/miscellaneous/ffmpeg/meshlabsmoothing/>
- ²⁵ https://slicer.readthedocs.io/en/latest/user_guide/modules/segmenteditor.html#smoothing
- ²⁶ <https://computergraphics.stackexchange.com/questions/11088/why-do-obj-files-contain-so-many-duplicate-vertices-if-they-use-indices-to-define>
- ²⁷ https://en.wikipedia.org/wiki/Neo-Hookean_solid
- ²⁸ <https://www.continuummechanics.org/mooneyrivlin.html>
- ²⁹ <https://vdocuments.net/ansys-hyperelastic-curve-fitting.html>

³⁰ <https://onscale.com/blog/meshing-in-fea-introduction-to-meshing/>

³¹ <https://abaqus-docs.mit.edu/2017/English/SIMACAEGSARefMap/simagsa-ctmmeshconverg.htm>

³² <https://abaqus-docs.mit.edu/2017/English/SIMACAEMATRefMap/simamat-c-hyperelastic.htm>

³³ <https://www.mechead.com/what-is-large-deflection-in-ansys/>

³⁴ vcg.isti.cnr.it/corsi/G3D_InfoUma/Slides_2020/05_MESH_EDITING.pdf